

# Study on Non-Linear Effects of Photoluminescence from Single-Walled Carbon Nanotubes

(単層カーボンナノチューブからの蛍光発光  
に対する非線形効果に関する研究)

Tokyo University of Science  
Department of Physics

Takumi Inaba  
(稲葉 工)

Date Submitted: 2015/12/7

# Abstract

Single-walled carbon nanotubes (SWCNTs) attract many researchers' attention with the expectation of those application to optoelectronic devices. Emission intensity of photoluminescence from SWCNTs is of great importance for the application. Photoluminescence intensity generally shows non-linear behavior as excitation intensity increases. Exciton-exciton annihilation, an Auger process of two excitons which results in the saturating behavior on photoluminescence intensity, can be firstly observed as excitation intensity increases. The diffusive motion of excitons is responsible for the two-body annihilation. Exciton diffusion length is a dominant physical parameter determining diffusive motion of excitons in SWCNTs. Exciton diffusion length has been reported by pump-probe method employing surfactant wrapped SWCNTs leaving the possible extrinsic effect caused by surfactant wrapping. Intrinsic and extrinsic effects should be properly distinguished for good understanding of the physics as well as the precise control of the nanotube devices. Further increasing excitation intensity causes the irreversible degrading of photoluminescence intensity such as photoinduced bleaching. The photoinduced bleaching of photoluminescence from SWCNTs rules the maximum excitation intensity for nanotube optoelectronic devices. Therefore, the origin of the photoinduced degradation should be clarified. And if possible, the recovery of photoluminescence intensity should be established.

In this thesis, non-linear effects on the photoluminescence from suspended SWCNTs are mainly discussed. The intrinsic diffusion length of SWCNTs was estimated to approximately 200 nm by analyzing the length dependence of photoluminescence intensity. Critical exciton density at which exciton-exciton annihilation occurs was estimated from the excitation power dependence of the intrinsic diffusion length. Newly developed Monte Carlo simulation verified the obtained results. Atmospheric ions, especially hydronium ions, along with hydrating water molecules in air were attributed to major chemical species causing photoinduced bleaching. The effect of photoexcitation to the reaction between atmospheric ions and SWCNTs was also proposed. A possible methodology for the recovery from degraded photoluminescence intensity was suggested from the origin.

The knowledge of exciton diffusion in SWCNTs is necessary for good understandings of their excited states caused by not only optical but also electronical means. Results obtained here contribute to developing the variety of nanotube optoelectronic devices especially by the improvement of

emission intensity. The realization of electroluminescence devices based on SWCNTs with intense luminescence, for example, will be essential technology for future information network. The effective use of excitons in SWCNTs also realizes the improvement of light harvesting devices.

# Frontispiece

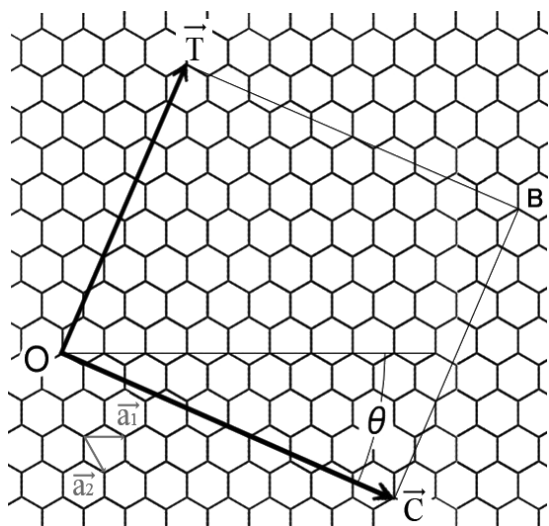


Fig. F1 Development view of primitive unit cell of a (6,4) nanotube.

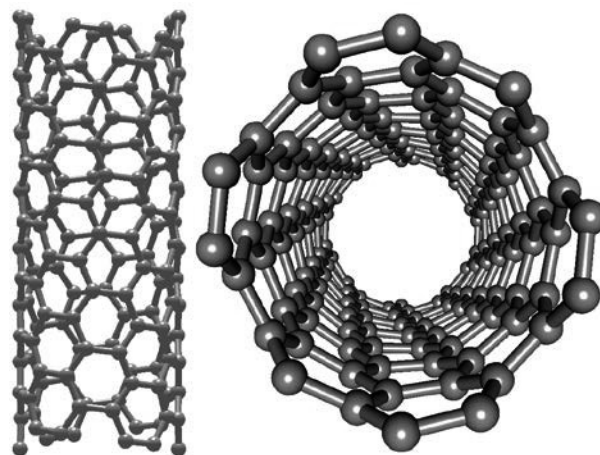


Fig. F2 Primitive unit cell of (6,4) nanotube.

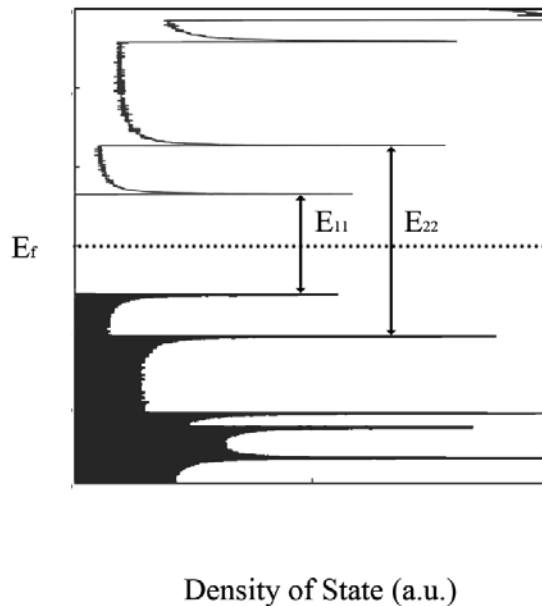
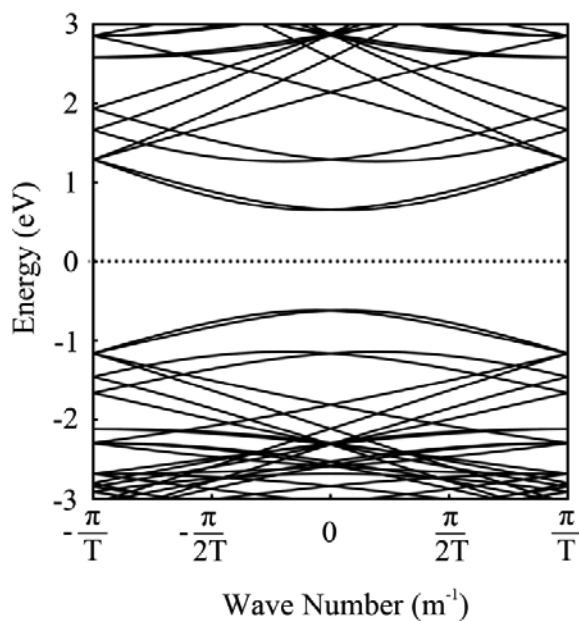


Fig. F3 Energy dispersion relation (Left) and corresponding DoS of the (6,4) nanotube.

# Table of Contents

<b>1</b>	<b>Introduction.....</b>	<b>1</b>
1.1	Single-Walled Carbon Nanotubes.....	1
1.2	Application to Optoelectronic Devices.....	1
1.3	Photoluminescence from Single-Walled Carbon Nanotubes.....	2
1.4	Excitons in Single-Walled Carbon Nanotubes.....	2
1.5	Non-Linear Behavior of Photoluminescence Intensity.....	4
1.6	Object of This Thesis.....	8
1.7	Outlines.....	9
<b>2</b>	<b>Experimental Method.....</b>	<b>13</b>
2.1	Sample Preparation.....	13
2.2	Optical Measurement Setup.....	16
2.3	Generation of Atmospheric Ions.....	18
<b>3</b>	<b>Intrinsic Exciton Diffusion Length and Exciton-Exciton Annihilation.....</b>	<b>21</b>
3.1	Introduction.....	21
3.2	Experiment.....	22
3.3	Length Dependence of Photoluminescence Intensity.....	23
3.4	Intrinsic Diffusion Length of Exciton in Single-Walled Carbon Nanotubes.....	26
3.5	Onset Power for Exciton-Exciton Annihilation; Analysis of Experimental Results.....	28
3.6	Onset Power for Exciton-Exciton Annihilation; Numerical Simulations.....	30
3.7	Summery.....	33
<b>4</b>	<b>Atmospheric ions as the origin of Photoinduced Degradation.....</b>	<b>36</b>

4.1	Introduction.....	36
4.2	Experiment.....	36
4.3	Degradation due to Exposure to High Atmospheric Ion Flux.....	37
4.4	Acceleration of the Reaction by the Excitation of Single-Walled Carbon Nanotubes.....	39
4.5	Reduction of Photoluminescence Intensity due to Exciton Localization.....	40
4.6	Low Energy Shift of Photoluminescence Peak Position due to the Attachment of Water Cluster Ions.....	42
4.7	Hydronium ion as Proton Donor.....	42
4.8	Effect of Laser Illumination.....	43
4.9	Discussion on Photoinduced Blinking.....	45
4.10	Recovery from Degraded Photoluminescence.....	45
4.11	Summery.....	47
<b>5</b>	<b>Conclusion and Outlook.....</b>	<b>50</b>

# Chapter 1

## Introduction

### 1.1 Single-Walled Carbon Nanotubes

Single-walled carbon nanotubes (SWCNTs) are fascinating materials. They are one of the carbon allotropes with quasi one dimensional (1D) structure firstly reported in 1993 [1]. They are made of single layer carbon atom honey-comb lattice, and have tubular structure with a few nanometer diameter. Covalent bonds with  $sp^2$  configurations compose their structures and make them the toughest, but flexible, materials on the earth [2] [3]. Toughest bonds and completeness of lattice structure also realize high thermal conductivity of SWCNTs up to  $3 \times 10^3$  W/m·K [4][5]. A pi-electron is generated for every single carbon atom as a result of  $sp^2$  hybridization and dominates electronic properties of SWCNTs [6]. Electron transport in SWCNTs is determined by scattering by defects and phonons which results in resistance similar to that in bulk materials [7]. On the other hand, reduced electron density of state for scattering which is expected for 1D materials [8], dissipation of back scattering due to the symmetry of the band structure [9], weak electron-acoustic-phonon interaction, and large optical phonon energy suppress the scattering rate of pi-electrons in SWCNTs. As a result, most cases, pi-electron in SWCNTs is ballistic over the length of modern scaled electronic devices [7]. Intrinsic electron mobility for semiconducting SWCNTs was estimated to be as high as  $10^5$   $cm^2/V \cdot s$  [10]. Physical properties of SWCNTs are superior to other nanoscale materials for future device applications. For example, thermal and electron conductivity of SWCNTs is 2-3 orders of magnitude higher than that of silicon nano-wire [11][12]. The possible application of SWCNTs to electric devices such as field effect transistors [13] have attracted many researchers' attention since the finding of SWCNTs. SWCNTs are now one of the candidates for materials which realize "Beyond CMOS".

### 1.2 Application to Optoelectronic Devices

Electron conductivity of SWCNTs was firstly predicted with the tight binding model based on the single electron approximation [6], and varies from metallic to semiconducting depending on their chirality [14]; i.e. helical arrangement of honey-comb lattice with respect to their tube axis. Electrons in semiconducting SWCNTs can be excited by means of electrical or optical way because they have a direct band gap with gap energy of c.a. 1 eV. Thus, emission wavelength of semiconducting SWCNTs is in the near infrared region, close to telecom wavelength. For this reason, the possible application of SWCNTs to a nano-scale light source which can be used for future information and communication technology have attracted many researchers [15]. When the optoelectronic application of SWCNTs is realized, communication devices will be further miniaturized, lower energy consumed, and faster operated. Recent research trend for all optical switching [16] also increases the importance of the nanotube researches aiming for the application to nano-scale light source because,

even if the logic circuit is driven by light, electron-photon conversion is necessary especially when the power of such devices is supplied by electricity, or in the situation where the devices are connecting other devices with wireless network. Furthermore, recent researches showed photon-antibunching of photoluminescence (PL) from SWCNTs [17][18]. Photon-antibunching is the physical phenomenon that photons are emitted singly and basic principle for the realization of information network based on quantum key. SWCNTs have enough ability as key materials for future information network technology.

### **1.3 Photoluminescence from Single-Walled Carbon Nanotubes**

Although photoexcitation of semiconducting SWCNTs had been expected from energy dispersion calculated by tight binding method, the experimental researches on the luminescence from SWCNTs have started after a nearly decade from its calculation. Photoluminescence from semiconducting SWCNTs is firstly observed in 2002 by isolating individual SWCNTs [19]. As-grown SWCNTs, in many cases, aggregate each other and those “bundled” SWCNTs do not show PL due to the charge transfer to metallic SWCNTs. In the first report of PL observation, sodium dodecyl sulfate (SDS) was employed as the surfactant for dissociation of nanotube bundles. Therefore, each SWCNTs prepared by the method was wrapped with SDS. Soon after the first observation of PL, new growth technique in which isolated SWCNTs were directly grown was proposed [20]. Special substrates with micro-pillars for suspending SWCNTs were prepared in the technique (See chapter 2 for detailed growth method). For instance, micro-pillars with a height of 10  $\mu\text{m}$  and a top diameter of 2  $\mu\text{m}$  were patterned on the substrate, and individual SWCNTs suspended between two micro-pillars. This kind of the nanotube sample is called air suspended SWCNT, or simply, suspended SWCNT. Suspended SWCNTs have the contact only with micro-pillar at their edges. Therefore, photoexcited charges do not transfer to other materials and intense PL from the SWCNT can be observed. Isolation with surfactant is now widely employed because of the easiness for sample preparation. Suspended SWCNTs, on the other hand, are used for the acquisition of more intrinsic nature of SWCNTs because suspended SWCNTs are free from surfactants or any other materials which would perturb the intrinsic nature of SWCNTs.

### **1.4 Excitons in Single-Walled Carbon Nanotubes**

It is well known that the binding energy of an exciton, an electron-hole pair, is infinity in pure 1D structure [21]. Single-walled carbon nanotubes have quasi 1D structure and exciton binding energy in SWCNTs is large enough for exciton to stably exist at room temperature [22][23]. As a result, oscillator strength for excitonic emission is more dominant than that for non-interacting particles [23]. The importance of exciton in energetically excited SWCNTs was pointed out in 1997 [22], but less attention was paid for excitons in SWCNTs at that time. Intensive studies on excitons in SWCNTs have been carried out after the first experimental observation of PL [23][24]. One of the important achievements done by earlier theoretical studies on excitons in SWCNTs is the successful description

of ratio problem [28][25]. In the tight binding model based on the single electron approximation, as a result of 1D structure of SWCNTs, divergence referred to as van Hove singularity (vHs) can be seen on the electron density of state. Optical excitation from  $i^{\text{th}}$  vHs at valence band to  $j^{\text{th}}$  vHs at conduction band is called  $E_{ij}$  excitation in carbon nanotube optoelectronics. Ratio problem is the discrepancy between the ratio of  $E_{22}$  to  $E_{11}$  excitation energy obtained from PL experiment and that expected from the tight binding model based on single electron approximation. Experimentally obtained  $E_{22}/E_{11}$  value is slightly lower than expected from the tight binding model as a result of many body effect. After some theoretical studies, experimental evidence of exciton formation in optically excited SWCNTs was confirmed by two-photon experiments [26][27]. Since then, the importance of many body effect for understanding the optical properties of SWCNTs has widely been known [28].

Generally, excitons in SWCNTs are generated by optical means in fundamental research while exciton generation by electron-hole impact induced by bias voltage along the nanotube axis is also possible [15] because SWCNTs have ambipolar transport. When excitons are generated via  $E_{22}$  optical excitation, which is often employed for optical measurements because of the good matching to visible to near infrared light source, phonon assisted relaxation to  $E_{11}$  subband soon occurs within approximately 40 fs creating  $E_{11}$  excitons [29]. Total energy of  $E_{11}$  exciton can be calculated from Bethe-Salpeter equation which describes two body bound states [30]. Ab-initio Green's function theory predicted that repulsive force, electron-hole exchange term in many body effect or simply electron-electron repulsion, is dominant in SWCNTs compared to attractive force as a result of the introduction of Coulomb interaction [24]. In other words, band gap enhancement exceeds exciton binding energy [22]. The total energy of  $E_{11}$  excitons is larger than  $E_{11}$  continuum by a few tens of meV [22][23][24] as a result of the introduction of Coulomb interaction. The derivation of exciton energy from Bethe-Salpeter equation also proposes the presence of exciton manifolds; i.e. fine structures of exciton state [31][32]. Due to the presence of time reversible symmetry on the graphene Brillouin zone, K and K' points, and spins of electron and hole, there are 16  $E_{11}$  exciton states [32]. Among 16 states, only one exciton with spin singlet and satisfying momentum conservation is optically allowed, thus the bright exciton. Energy of ground state for excitons in the manifold differs each other slightly. For example, excitons with the symmetry under the turning over of the nanotube axis has ground state 12 meV below the antisymmetric bright exciton while the triplet state lies 35 meV below the bright state [31]. Brightening of those dark excitons occur when the symmetry is broken [33] or spin-orbit interactions are enhanced [34]. Coulomb interaction defines excitonic effects in SWCNTs. Thus, optical properties of SWCNTs largely depend on dielectric environment around them [35][36]. It is worth mentioning that wave functions of excitons were also derived by solving Bethe-Salpeter equation of the two-particle Green's function, from which the size of exciton was estimated to approximately 2 nm [24].

Lifetime  $\tau$  of  $E_{11}$  exciton is the order of a few tens of ps at room temperature [37].  $E_{11}$  excitons diffuse in SWCNTs within their lifetimes. Up to now, many experimental studies have been carried out to investigate the exciton diffusion length in semiconducting SWCNTs leaving large scattering

values. The diffusion length of excitons differs by several orders of magnitude ranging from  $10^0$  to  $10^2$  nm [38]-[43]. The scattering is possibly due to difference in the sample preparation method for each experiment which would determine the sample properties such as the dielectric environment around SWCNTs or the number of defects induced in SWCNTs, and so on. Lifetime, as well as diffusion length, of excitons is a consequence of how the exciton decays. There are some possible decay paths for excitons in SWCNTs. The most simple and clear one is radiative decay in which the exciton decays with emitting a single photon. Radiative lifetimes ranging from 3 to 10 ns was estimated from simultaneous measurement of PL lifetimes and PL quantum yields (QYs) [44], which is corresponding to radiative decay rate  $k_r$  of 0.1 to 1 ns<sup>-1</sup>.

Nonradiative decay is even more complex because several decay paths are possible. Especially when holes are doped to SWCNTs, phonon assisted indirect exciton ionization (PAIEI) is the possible mechanism for nonradiative decay [45]. An exciton nonradiatively decays in PAIEI creating an intraband electron-hole pair and a phonon. Decay time for PAIEI at doping level of +0.21 e/nm is ranging from 8 to 40 ps depending on exciton energy. The larger exciton energy, the larger decay time, thus the smaller decay rate. Decay time for PAIEI also depends on exciton manifold. For example, smaller decay time is expected for the lowest energy dark exciton. In addition to PAIEI, multi phonon decay (MPD) was also proposed to as the possible mechanism of exciton decay [45]. An exciton decays into its ground state emitting phonons. Although relaxation via MPD is reasonable in SWCNTs because of the presence of high energy phonon such as in-plane lattice oscillation of sp<sup>2</sup> honey comb lattice (G-mode), calculation revealed that only excitons in SWCNTs with the diameter larger than 1.4 nm are effectively annihilate via MPD. Interestingly, the nonradiative decay lifetime of MPD decreases for localized exciton as a result of enhanced exciton-phonon coupling due to the reduced exciton dispersion of bound excitons. In that case, excitons in SWCNTs with the diameter of approximately 1 nm are also effectively annihilate via MPD. Therefore, MPD is possible mechanisms of exciton annihilation at “quench points” in SWCNTs while PAIEI is more general decay path for excitons diffusing in SWCNTs. As shown later, exciton-exciton annihilation (EEA) is also one of the nonradiative decay paths for excitons in SWCNTs. The total lifetime  $\tau$  of excitons is determined from those decay rates as:  $\tau = (k_r + k_{nr})^{-1}$ . Therefore, nonradiative decay is the dominant mechanism determining the total lifetime  $\tau$  of excitons in SWCNTs.

### 1.5 Non-Linear Behavior of Photoluminescence Intensity

Lattice structures of SWCNTs are not only beautiful but also useful for the future information network technology. However, one cannot receive full benefit of those fascinating materials without overcoming some challenges. One of such challenges is controlling emission properties of SWCNTs. Especially, the factors determining PL intensity should be well understood for optoelectronic applications. Assuming the situation where SWCNTs are applied to electron-photon conversion unit embedded in mobile devices, the higher emission intensity, the lower energy consumption, which means the longer working time within limited capacity of battery. Fields that SWCNTs can be applied

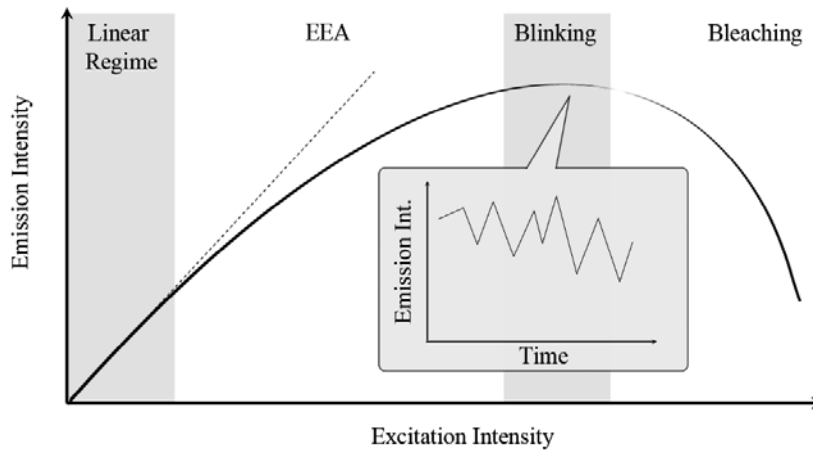


Fig. 1.1 Schematic drawing of emission intensity as a function of excitation intensity.

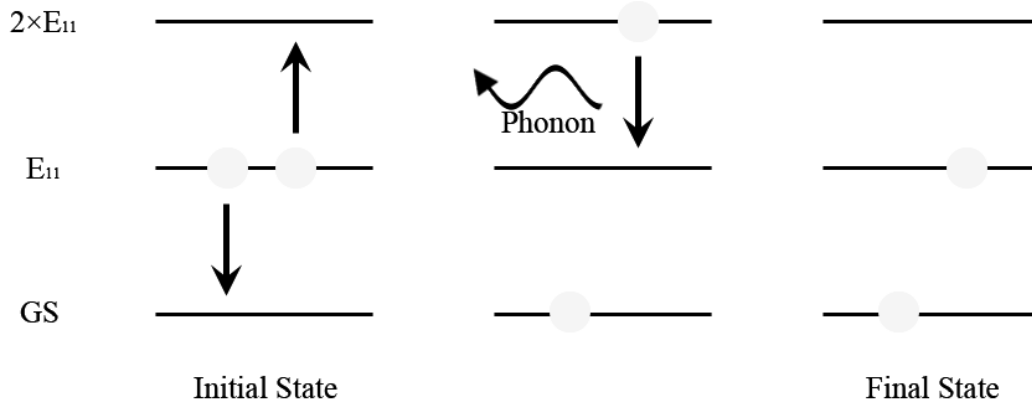


Fig. 1.2 Schematic drawing of EEA process.

to also expands as the emission intensity increases. Unfortunately, quantum yield of SWCNTs is not so large. Quantum yield of 7 % for suspended SWCNTs was experimentally deduced [46], which is relatively larger value among the nanotube sample used in PL experiment. On the other hand, quantum yields below 1% have been reported for surfactant wrapped nanotube samples [47]. Even if SWCNTs are strongly excited in order to get stronger emission intensity, the intensity does not increase as expected because of non-linear behavior such as EEA [48][49], photoinduced blinking, and photoinduced bleaching [51][54].

Exciton-exciton annihilation is an Auger process of two excitons as shown in Fig. 1.2 [48]. When two excitons approach each other within reaction radius, one of the excitons decays resulting in the creation of an exciton in a higher energy state. The resulting exciton at the higher energy state then emits phonons and returns to its original state. This process finally causes a single exciton in original state and the other in ground state. The possibility that excitons are in reaction radius

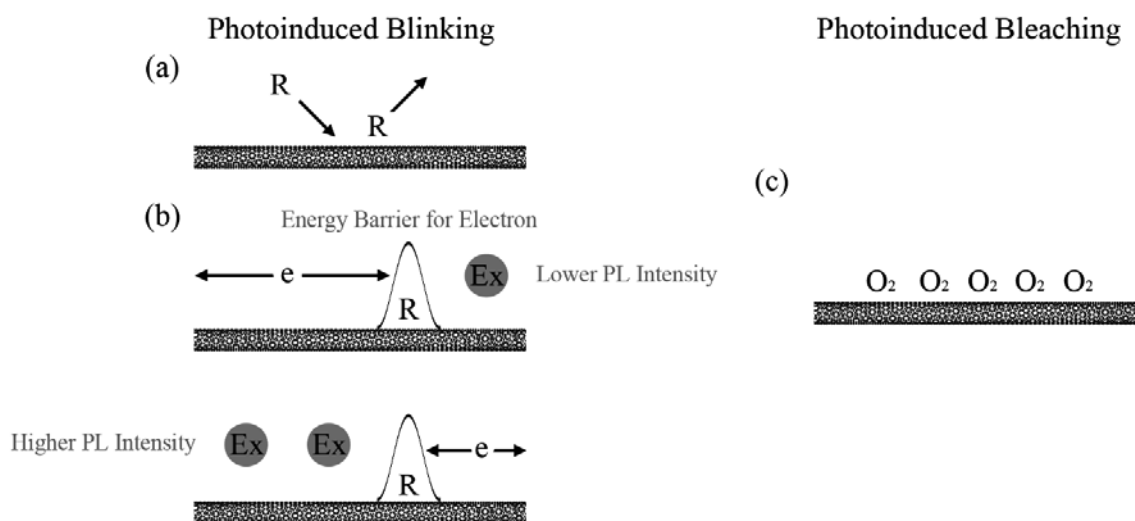


Fig. 1.3 Schematic drawing of possible mechanisms for blinking (a, b) and bleaching (c). The label “R” represents unknown reaction species, the label “e” a mobile electron, and the label “Ex” a diffusive exciton.

increases as excitation intensity increases. Thus, PL intensity deviates from the linear fitting line of low excitation regime (Fig. 1.1). Exciton-exciton annihilation has been studied in previous researches revealing maximum exciton density in SWCNTs. As a result, maximum exciton density lower than expected Mott density was obtained [55]. Diffusion of excitons in SWCNTs is probably the cause of the lower maximum density. Most researches reporting EEA have relied on time-dependent observation such as transient absorption or transient PL spectroscopy [55]-[57]. Monte Carlo simulation, which is tuned for the verification of results obtained by transient fluorescent experiments, has also been employed. On the other hand, experimental results based on continuous wave (CW) excitation as well as CW oriented simulation were hardly seen. This is possibly due to the difficulty in analyzing non-linear dynamics of EEA. For example, analytical and numerical calculations are less complex for a pump-probe like method where excitons are generated at a time. On the other hand, calculations are more difficult for regenerating a CW like experiment with non-linear behavior such as EEA, which results in less reports dealing with EEA under CW excitation. Furthermore, SWCNTs with surfactant wrapping that hide the intrinsic nature have been employed especially for transient absorption or PL spectroscopy. Therefore, intrinsic parameters relating to exciton diffusion, such as diffusion length or their lifetime, are still not clear.

Photoinduced blinking is the time dependent fluctuation of PL intensity as shown in the inset of Fig. 1.1. For SWCNTs showing photoinduced blinking, the fluctuation of PL intensity is observed despite fixed excitation intensity. Photoinduced blinking is often seen in advance of photoinduced bleaching as excitation intensity of SWCNTs increases [51][54]. Photoinduced blinking can be observed in air with the excitation intensity over 20 kW/cm<sup>2</sup> for surfactant wrapped SWCNTs [54].

Some researches attributed photoinduced blinking to reversible physisorption [51] or irreversible chemisorption [54] of oxygen to the nanotube surface. However, the number of experimental reports discussing photoinduced blinking in air is still small and there is no comprehensive understanding for the mechanism.

It is worth mentioning that the fluctuation of PL intensity was also reported for the surfactant wrapped SWCNTs in aqueous solution [38][58]. The generation of quench point for mobile exciton induced by reversible attack of chemical species to the nanotube surface, as shown in Fig. 1.3a, was attributed to the fluctuation of PL intensity in some papers [38]. Here, the label “R” in Fig. 1.3a represents unknown reaction species. On the other hand, another paper argued that the chemical attack is completely irreversible, and mobile charges induced by the chemical attack is responsible for the fluctuation of PL intensity as shown in Fig. 1.3b [58]. Here, the labels “e” and “Ex” in Fig. 1.3b represent a mobile electron and a diffusive exciton, respectively. In the latter case, mobile charges go around in an SWCNT that has some energy barriers induced by irreversible chemical bonding. For example, if the SWCNT is divided into two segments with different lengths by a single energy barrier, and a mobile charge is found in the SWCNT, overall PL intensity depends on where the mobile charge is. This is because PL from a segment where the mobile charge is located decreases due to PAIEI [45]. Relatively higher overall PL intensity is expected when the mobile charge is at the shorter nanotube segment, thus PAIEI occurs at the shorter segment, because higher PL from longer segment is preserved; intrinsic PL intensity depends on the segment length [59]. On the other hand, lower PL intensity would be obtained when the mobile charge is at the longer segment. The description of PL blinking with mobile charges is consistent with spatially correlated PL intensity observed in some reports [51][58]. Although those proposed mechanisms for the fluctuation of PL intensity from SWCNTs in aqueous solution were not photoinduced effects, parts of those mechanisms are applicable to the photoinduced blinking in air.

Photoinduced bleaching occurs when SWCNTs are photoexcited by intense laser light typically over  $100 \text{ kW/cm}^2$ . Photoinduced bleaching in this thesis does not refer to the temporal bleaching of absorption; i.e. phase space filling. Photoinduced bleaching is irreversible and permanent weakening of PL intensity accompanied by the low energy shift of PL peak position. For example, once SWCNTs suffer photoinduced bleaching, PL intensity at linear regime also gets lower than its original value. Furthermore, photoinduced bleaching of PL from SWCNTs occurs much lower excitation intensity than that for the bleaching of absorption. In fact, Raman spectra can be obtained even after the complete loss of PL intensity due to photoinduced bleaching. Although plausible photoinduced mechanisms and possible chemical bonding form are not known yet, photoinduced bleaching are often attributed to the attachment of oxygen in air on the nanotube surface (Fig. 1.3c). The reduction of PL intensity due to the attachment of molecule on the nanotube surface is reasonable. For example, it is well known that PL intensity from nanotube samples that are prepared by surfactant wrapping is generally lower than PL intensity from air suspended SWCNTs. Satellite peaks at low energy side of main PL peak position were also observed for degraded SWCNTs [50][51]. The emergence of satellite

peaks evokes the brightening of dark exciton states. The brightening of dark excitons is often observed with perturbed SWCNTs. For example,  $sp^3$  hybridization of carbon atoms in SWCNT enhances spin-orbit interaction which is usually negligible for SWCNTs because of small mass of a carbon atom [52]. As a result of the enhanced spin-orbit interaction, dark triplet exciton state located energetically below bright singlet exciton state turns to optically-allowed. Some researches attributed the partial  $sp^3$  hybridization of carbon atoms to the hydrogen adsorption onto the nanotube surface [34][53]. The emission from the dark triplet exciton state was observed approximately 65 meV lower to the emission from the bright singlet exciton in the hydrogen adsorption experiment [34]. While the diameter dependence of the separation between the bright singlet and dark triplet exciton state was claimed, the scattering of satellite peak position was observed even for a single SWCNT suffering photoinduced degradation [51]. The difference in chemical species may be accounted for the scattering of satellite peak position. Similar to blinking of PL from SWCNTs in aqueous solution, bleaching was also observed in solution based experiment by acidification [60]. In the PL bleaching experiment in aqueous solution, both high and low energy shift of peak position were observed. On the other hand, photoinduced bleaching in air is often accompanied by low energy shift of PL peak position and high energy shift of peak position is hardly observed.

## **1.6 Object of This Thesis**

This thesis covers the discussion on the emission intensity of PL from suspended SWCNTs and provides;

### **First observation of Well-Defined Diffusion Length**

Exciton diffusion length is one of the important parameters determining optical properties of SWCNTs. When single photon emission is expected, for example, the length of SWCNTs is defined by exciton diffusion length. Relation between nanotube lengths and exciton concentration, thus length dependent PL intensity, are necessary for extracting the diffusion length from the 1D diffusion equation. So far, surfactant wrapped SWCNTs have been frequently employed for the derivation of diffusion length because of the easiness of preparing a length and chirality sorted sample. However, surfactants probably perturb the intrinsic nature of SWCNTs. In fact, exciton binding energy decreases due to dielectric environment made by surfactant. Furthermore, the attachment of surfactants onto the nanotube surface would possibly induces non-radiative decay paths for excitons. Therefore, intrinsic exciton diffusion length cannot be obtained for surfactant wrapped SWCNTs. On the other hand, intrinsic exciton diffusion length was obtained in this thesis with the SWCNT suspended on the groove patterned substrate on which grooves with some different widths were patterned.

### **Onset Power for Exciton-Exciton Annihilation**

Exciton-exciton annihilation, which is an Auger process of two exciton, causes non-linear behavior

on the relation between emission and excitation intensity. The derivation of critical exciton density at which EEA occurs gives important information for not only exciton photophysics in SWCNTs but also for the application of SWCNTs to optoelectronic devices. For example, quantum yields of PL from SWCNTs are probably lowered from intrinsic value when the excitation intensity larger than the critical excitation intensity for EEA is employed. Furthermore, device design for single exciton devices is ruled by exciton density in SWCNTs. The dynamics of exciton, including EEA, has been often reported with pump-probe method while validity for CW excitation is lacking. In this thesis, multilateral analysis for extracting the critical exciton density for EEA with CW excitation was firstly proposed. The critical exciton density for EEA was estimated not only from experiments but also from Monte Carlo simulation (MCS) in order to verify the obtained experimental data. Internal quantum yields was also derived from the MCS developed here.

### **Revealing the Origin of Photoinduced Degradation**

Photoinduced degradation, thus blinking and bleaching, defines the maximum excitation intensity available for retaining intrinsic optical properties of SWCNTs. The lifetime of optoelectronic devices employing SWCNTs is also ruled by photoinduced degradation because photoinduced degradation possibly occurs even at low excitation regime by accumulating time. The assignment of reaction species as well as possible mechanisms should be well understood for sustaining intrinsic properties of SWCNTs. Recovery from degrading PL intensity is also meaningful for the nanotube research and its application to optoelectronic devices. In this thesis, the attachment of atmospheric ion along with hydrated water molecules onto the nanotube surfaces were attributed to the origin of photoinduced degradation. No other reports have paid attention to the ionic species in air as the origin of photoinduced degradation resulting in missing possible mechanisms where PL intensity degrades by photoexcitation. The assignment of the origin allowed us to assume the possible mechanism for the photoinduced degradation. Furthermore, the recovery of original PL intensity was tested from the assumption of the possible origin.

### **1.7 Outlines**

Experimental method and equipment employed for experiments are briefly introduced in chapter 2. Homemade optical setup for PL and Raman spectroscopy is also referred to there. The air ionizer used for the generation of atmospheric ions and brief introduction of atmospheric ions are presented.

Chapter 3 gives the discussion of diffusive excitons in long suspended SWCNTs. Intrinsic exciton diffusion length is estimated from the length dependent PL from long suspended SWCNTs. The critical excitation intensity for EEA is also derived from the dependence of diffusion length. In addition to experimental results already reported, 1D MCS newly developed for exciton diffusion in SWCNTs and the some results are shown in chapter 3.

In chapter 4, degrading of PL intensity due to the attachment of atmospheric ions is discussed. The effects of laser illumination to the reaction is shown, and the possibility that the reaction is

responsible for the origin of photoinduced degradation of PL from SWCNTs in air is proposed. Possible mechanisms for the attachment of atmospheric ions, as well as the recovery of original PL intensity are also discussed there.

Chapter 5 gives conclusion of the thesis. Outlook for future study with the discussion of recent trend in the researches on optical properties of SWCNTs is also indicated in chapter 5.

## References

- [1] S. Iijima, T. Ichihashi, *Nature* 363, 603 (1993)
- [2] C. Li, T-W. Chou, *Int. J. Solids. Struct.* 40, 2487 (2003)
- [3] L. Shen, and J. Li, *Phys. Rev. B* 69, 045414 (2004)
- [4] A. M. Marconnet, M. A. Panzer, and K. E. Goodson, *Rev. Mod. Phys.* 85, 1295 (2013)
- [5] E. Pop, D. Mann, Q. Wang, K. Goodson, and H. Dai, *Nano Lett.* 6, 96 (2006)
- [6] R. Saito, M. Fujita, G. Dresselhaus, and M. S. Dresselhaus, *Appl. Phys. Lett.* 60, 2204 (1992)
- [7] P. Avouris, Z. Chen, and V. Perebeinos, *Nature Nanotech.* 2, 605 (2007)
- [8] H. Sasaki, *Jpn. J. Appl. Phys.* 19, L735 (1980)
- [9] T. Ando, and T. Nakanishi, *J. Phys. Soc. Jpn.* 67, 1104 (1998)
- [10] T. Durkop, S. A. Getty, Enrique Cobas, and M. S. Fuhrer, *Nano Lett.* 4, 35 (2004)
- [11] O. Gunawan, L. Sekaric, A. Majumdar, M. Rooks, J. Appenzeller, J. W. Sleight, S. Guha, and W. Haensch, *Nano Lett.* 6, 1096 (2008)
- [12] D. Li, Y. Wu, P. Kim, L. Shi, P. Yang, and A. Majumdar, *Appl. Phys. Lett.* 83, 2934 (2003)
- [13] P. Avouris, *Phys. Today* 62, 34 (2009)
- [14] N. Hamada, S. Sawada, and A. Oshiyama, *Phys. Rev. Lett* 68, 1579 (1992)
- [15] P. Avouris, *Nature Photon.* 2, 341 (2008)
- [16] V. R. Almeida, C. A. Barrios, R. R. Panepucci, and M. Lipson, *Nature* 431, 1081 (2004)
- [17] A. Högele, C. Galland, M. Winger, and A. Imamoğlu, *Phys. Rev. Lett.* 100, 217401 (2008)
- [18] T. Endo, J. Ishi-Harase, and H. Maki, *Appl. Phys. Lett.* 106, 113106 (2015)
- [19] M. J. O'Connell, S. M. Bachilo, C. B. Huffman, V. C. Moore, M. S. Strano, E. H. Heinz, K. L. Rialon, P. J. Boul, W. H. Noon, C. Kitterell, J. Ma, R. H. Hauge, R. B. Weisman, R. E. Smalley, *Science* 297, 593 (2002)
- [20] J. Lefebvre, Y. Homma, P. Finnie, *Phys. Rev. Lett.* 90, 217401 (2003)
- [21] Y. Zhang, and A. Mascarenhas, *Phys. Rev. B* 59, 2040 (1999)
- [22] T. Ando, *Jpn. J. Phys. Soc.* 66, 1066 (1997)
- [23] V. Pereveinos, J. Tersoff, and P. Avouris, *Phys. Rev. Lett.* 92, 257402 (2004)
- [24] C. D. Spataru, S. Ismail-Beigh, L. X. Benedict, and S. G. Louie, *Phy. Rev. Lett.* 92, 077402 (2004)
- [25] C. L. Kane, E. J. Mele, *Phys. Rev. Lett.* 90, 207401 (2003)
- [26] F. Wang, G. Dukovic, L. E. Brus, T. F. Heinz, *Science* 308, 838 (2005)
- [27] J. Maultzsch, R. Pomraenke, S. Reich, F. Chang, D. Prezzi, A. Ruini, E. Molinari, M. S. Strano, C. Thomsen, and C. Lienau, *Phys. Rev. B* 72, 241402R (2005)

- [28] M. S. Dresselhaus, G. Dresselhaus, R. Saito, and A. Jorio, *Annu. Rev. Phys. Chem.* 58, 719 (2007)
- [29] C. Manzoni, A. Gambetta, E. Menna, M. Meneghetti, G. Lanzani, and G. Cerullo, *Phys. Rev. Lett.* 94, 207401 (2005)
- [30] Y. Nambu, *Progress of Theoretical Physics* 5, 614 (1950).
- [31] J. Jiang, R. Saito, Ge. G. Samsonidze, A. Jorio, S. G. Chou, G. Dresselhaus, and M. S. Dresselhaus, *Phys. Rev. Lett.* 75, 035707 (2007)
- [32] T. Ando, and S. Uryu, *Phys. Stat. Sol.* 6, 173 (2009)
- [33] S. Zaric, G. N. Ostojic, J. Kono, J. Shaver, V. C. Moore, M. S. Strano, R. H. Hauge, R. E. Smalley, X. Wei, *Science* 304, 1129 (2004)
- [34] K. Nagatsu, S. Chiashi, S. Konabe, and Y. Homma, *Phys. Rev. Lett.* 105, 157403 (2010)
- [35] Y. Ohno, S. Iwasaki, Y. Murakami, S. Kishimoto, S. Maruyama, and T. Mizutani, *Phys. Rev. B* 73, 235427 (2006)
- [36] Y. Homma, S. Chiashi, T. Yamamoto, K. Kono, D. Matsumoto, J. Shitaba, and S. Sato, *Phys. Rev. Lett.* 110, 157402 (2013)
- [37] T. Gokus, A. Hartschuh, H. Harutyunyan, M. Allegrini, F. Hennrich, M. Kappes, A. A. Green, M. C. Hersam, P. T. Araujo, and A. Jorio, *Appl. Phys. Lett.* 92, 153116 (2008)
- [38] L. Cognet, D. A. Tsyboulshi, J.-D. R. Rocha, C. D. Doyle, J. M. Tour, and R. B. Weisman, *Science* 316, 1465 (2007)
- [39] L. Luer, S. Hoseinkhani, D. Polli, J. Chrochet. T. Hertel, and G. Lanzani, *Nature Phys.* 5, 54 (2009)
- [40] C. Georgi, M. Bohmler, H. Qian, L. Novotny, and A. Hirschuh, *Phys. Status, Solidi B* 246, 2683 (2009)
- [41] A. J. Siitonen, D. A. Tsyboulski, S. M. Bachilo, and R. B. Weisman, *Nano Lett.* 10, 1595 (2010)
- [42] S. Moritsubo, T. Shimada, Y. Murakami, S. Chiashi, S. Maruyama, and Y. K. Kato, *Phys. Rev. Lett.* 104, 247402 (2010)
- [43] K. Yoshikawa, K. Matsuda, and Y. Kanemitsu, *J. Phys. Chem. C* 114, 4353 (2010)
- [44] Y. Miyauchi, H. Hirori, K. Matsuda, and Y. Kanemitsu, *Phys. Rev. B* 80, 081410R (2009)
- [45] V. Perebeinos, and P. Avouris, *Phys. Rev. Lett.* 101, 057401 (2008)
- [46] J. Lefebvre, D. G. Austing, J. Bond, and P. Finnie, *Nano Lett.* 6m 1603 (2006)
- [47] T. Hertel, S. Himmelein, T. Ackermann, D. Stich, and J. Crochet, *ACS Nano* 4, 7161 (2010)
- [48] L. Valkunas, G. Trinkunas, V. Liiolia, and F Grondelle, *Biophys. J.* 69, 1117 (1995)
- [49] Y-Z. Ma, J. Stenger, J. Zimmermann. S. M. Bachilo, R. E. Smalley, R. B. Weisman, and G. R. Fleming, *J. Chem. Phys.* 120, 3368 (2004)
- [50] R. Matsunaga, K. Matuda, and Y. Kanemitsu, *Phys. Rev. B* 81, 033401 (2010)
- [51] P. Finnie, and J. Lefebvre, *ACS Nano* 6, 1702 (2012)
- [52] K. Matsuda, *Progress in Nanophotonics* 2, Springer Berlin Heidelberg, p. 48 (2013)
- [53] S. Konabe, and K. Watanabe, *Phys. Rev. B* 83, 045407 (2011)

- [54]C. Georgi, N. Hartmann, T. Gokus, A. A. Green, M. C. Hersam, and A. Hertschuh, *ChemPhysChem* 9, 1460 (2008)
- [55]A. Srivastava, and J. Kono, *Phys. Rev. B* 79, 205407 (2009)
- [56]L. Valkunas, *Phys. Rev. B* 73, 115432 (2006)
- [57]Y-Z. Ma, L. Valkunas, S. L. Dexheimer, S. M. Bachilo, and G. R. Fleming, *Phys. Rev. Lett.* 94, 157402 (2005)
- [58]J. J. Crochet, J. G. Duque, J. H. Werner, and S. K. Doorn, *Nature Nanotech.* 7, 126 (2012)
- [59]D. M. Harrah, and A. K. Swan, *ACS Nano* 5, 647 (2011)
- [60]G. Dukovic, B. E. White, Z. Zhou, F. Wang, S. Jockusch, M. L. Steigerwald, T. F. Heinz, R. A. Friesner, N. J. Turro, and L. B. Brus, *J. Am. Chem. Soc.* 126, 15269 (2004)

# Chapter 2

## Experimental Methods

In this chapter, information on the experimental method is introduced. Mainly two types of SWCNTs samples were prepared for this thesis. One was a long suspended SWCNTs on a groove patterned substrate. The other was a suspended SWCNTs grown a pillar patterned substrate. The former was employed for the experiment in chapter 3 because a single SWCNT suspended on grooves with different widths was needed there. The latter was, on the other hand, employed for the experiment in chapter 4. All of the SWCNTs shown in this thesis were grown by chemical vapor deposition (CVD). Home-made optical measurement setup employed for PL spectroscopy, PL imaging, and Raman spectroscopy is described. The air ionizer used for the generation of atmospheric ions in chapter 4 is also introduced in this chapter.

### 2.1 Sample Preparation

#### **Long Suspended Single-Walled Carbon Nanotubes on Groove Patterned Substrate**

There are mainly two steps for nanotube growth by CVD [1]. First step is deposition of metal on the supporting substrate. In this thesis, conventional vacuum deposition was employed for depositing metal on supporting substrates under the medium vacuum of 0.4 Pa. Deposited metal works as “catalysts” for nanotube growth by forming nano-particles under high temperature during CVD. For the growth of long suspended SWCNT, an iron thin layer with a submonolayer thickness was deposited on a thermally oxidized silicon substrate. Here, the amount of deposited metal was calibrated by chemical analysis using inductively coupled plasma mass spectroscopy.

The home-made CVD system composed of a container filled with ethanol as the carbon source, Ar/H<sub>2</sub>(3%) cylinders as the carrier gas, a horizontal quartz tube furnace, and a rotary pump were employed for nanotube growth. The illustration of the CVD system is shown in Fig. 2.1. Pressure and gas flow rate inside the quartz tube were controlled using the mass flow controllers (MFC) allocated in front of the quartz tube and the needle valve (NV) behind the quartz tube. Details of the CVD condition is shown in Fig. 2.2a. Chemical vapor deposition was carried out at atmospheric pressure. Bubbling to the ethanol container with carrier gas was conducted so that enough ethanol concentration in vapor could be obtained even at atmospheric pressure. The gas-flow method was employed for the growth of long suspended SWCNTs [2]. In the gas-flow method, SWCNTs grew without touching the substrate like a kite during CVD. After the growth, the quartz tube was cooled down with keeping filled with the carrier gas so that SWCNTs were not oxidized when the substrate was taken out from the chamber. The substrate was taken out from the quartz tube after the temperature was lower than 100 °C. Substrate configuration as shown in Fig. 2.3 was employed for the growth of SWCNTs used in this thesis. Two substrates were put in the quartz tube as shown in Fig. 2.3 so that the iron deposited

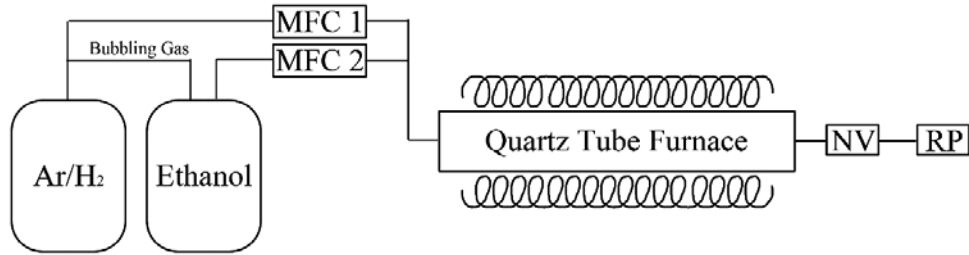


Fig. 2.1 Schematic drawing of the CVD system.

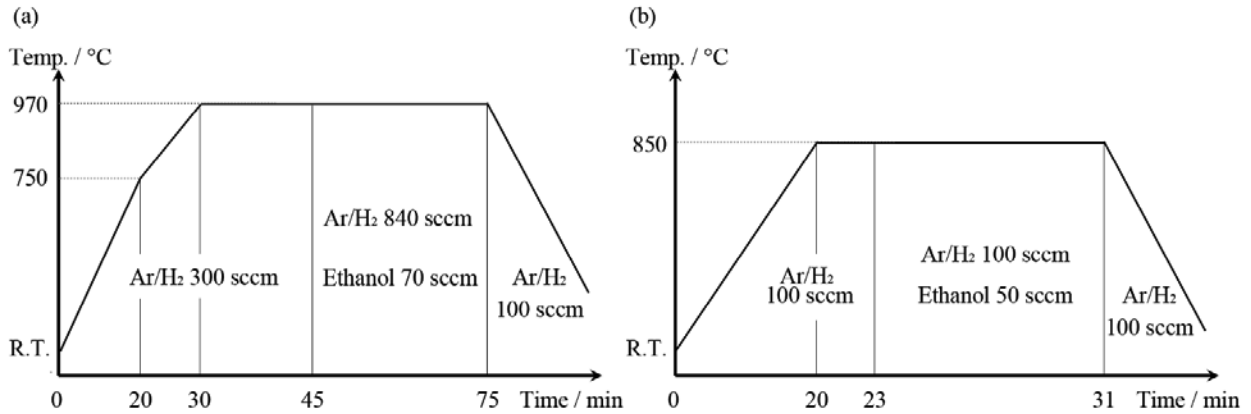


Fig. 2.2 (a) CVD condition used for the gas-flow growth and (b) that of suspended SWCNTs between micro-pillars

silicon oxide substrate was on the upper stream of the quartz tube, thus the groove patterned substrate on the downstream. Long SWCNTs grown on the iron deposited substrate extended to the other one by gas flow.

Scanning electron microscopy (SEM) was employed after CVD for brief verification of the nanotube growth. The acceleration voltage of electron beam was set as low as possible (0.5 kV) and observation was conducted in short time so that damage to SWCNTs due to electron beam irradiation was suppressed [3]. SEM images of SWCNTs are shown in Fig. 2.4. Figure 2.4a shows long SWCNTs grown by the gas-flow method with the partially-iron-deposited thermally oxidized silicon substrate. Iron was deposited at the left edge of the substrate. Gas flow directed from left to right during the CVD. The iron deposited area appears bright due to the massive electron emission from SWCNTs covering the area while the number of SWCNTs extended rightward is limited. Some SWCNTs with the length over 100  $\mu\text{m}$  can be observed in Fig.2.4a. A part of the long suspended SWCNT grown on the groove patterned substrate is shown in Fig. 2.4b. The lower illustration is the corresponding side view of the groove patterned substrate. The SWCNT was grown with the substrate configuration shown in Fig. 2.3 using thermally oxidized silicon substrate with iron deposition and groove patterned quartz substrate. While secondary electron emission from line segments of the SWCNT contacting with insulating quartz substrate was relatively large due to electron beam induced conductivity [4], that from suspended SWCNTs was relatively small in Fig. 2.4a. Because of this, the width of

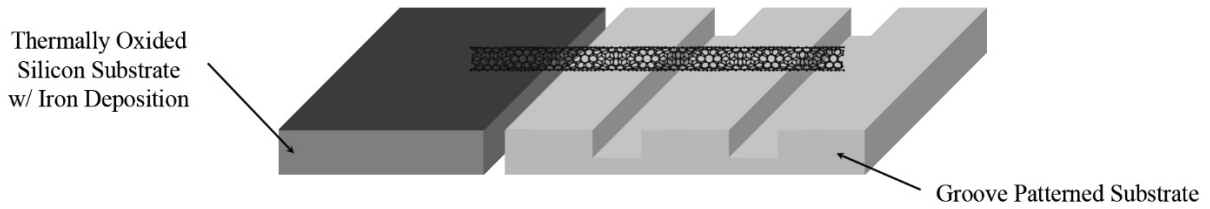


Fig. 2.3 Configuration of substrates for long suspended SWCNTs during CVD.

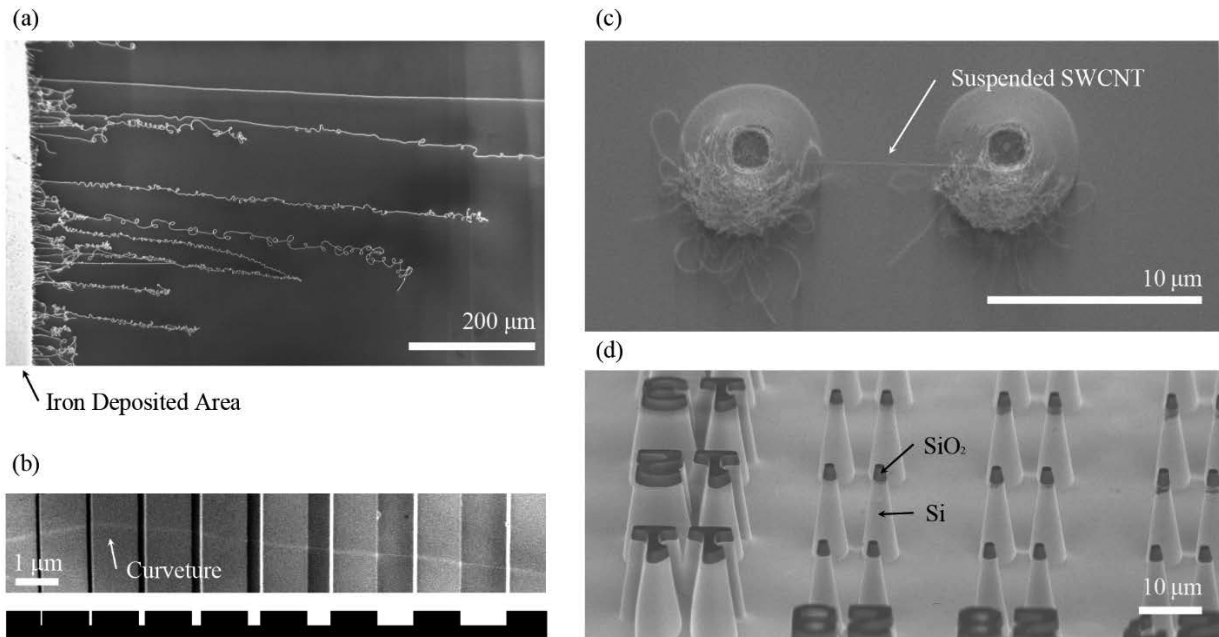


Fig. 2.4 (a) Long SWCNTs grown by gas-flow method on partially iron deposited substrates. Iron deposited area were totally covered with SWCNTs and was bright due to large amount of secondly electron emission. (b) A long suspended SWCNT on the groove patterned substrate grown by gas-flow method. The SWCNT suspended over many grooves with different widths. Lower inset is illustration of corresponding groove structure. (c) SWCNT suspended between two micro-pillars. Some SWCNTs grew from the top of pillars but only one SWCNT successfully suspended between those pillars. (d) Bird's eye view of a micro-pillar substrate. The substrate was made from quartz and silicon was deposited except the top of pillars.

SWCNTs on insulating substrates does not show actual diameter of SWCNTs.

### Suspended Single-Walled Carbon Nanotubes between Micro-Pillars

For optical measurements of SWCNTs, SWCNTs with the diameter of approximately 1 nm are favorable because  $E_{22}$  absorption of those SWCNTs is closed to 1.5 eV and effective optical excitation can be achieved using the Ti:sapphire laser system employed for optical measurements in this thesis. The diameter range of long suspended SWCNTs grown by the gas-flow method is generally centered

at 1.5 nm [5], and growth yield of SWCNTs with the diameter of approximately 1 nm was not so large. Furthermore, the position of long SWCNTs was randomly distributed, which resulted in the difficulty in positioning luminescent SWCNTs with focused laser light in optical measurements. Therefore, although gas-flow method was employed for obtaining “long” suspended SWCNTs above, such growth method was not suitable for optical measurements. For the growth of air suspended SWCNTs used in chapter 4, the CVD condition shown in Fig. 2.2b was employed along with the cobalt-deposited pillar-patterned substrate. The normal thickness of cobalt thin layer was 0.078 Å. The use of cobalt as catalysts, relatively lower temperature, and smaller amount of carbon source than gas-flow method supplied high growth yields of SWCNTs with the diameter of approximately 1 nm. Many pairs of pillars with the height of 10 µm and the separation of 10 µm were fabricated on the pillar patterned substrate. SWCNTs suspended only between those pillars, which made it easy to find luminescent SWCNTs with focused laser light [6]. In order to make suspended structure between two micro-pillars, SWCNTs grown on the top of a micro-pillar need to touch the top of the other micro-pillar before touching the pillar wall or elsewhere [7]. Indeed, many SWCNTs grew on the top of a single micro-pillar and most of them fell on the pillar wall without reaching the other micro-pillar. Some SWCNTs lifted up and reached to the other micro-pillar forming suspended SWCNTs. The process time of CVD was set to 8 min as shown in Fig. 2.2b so that the high growth yields of a singly suspended SWCNT for each pair of pillars was obtained. Longer process time may cause bundled suspended SWCNTs.

Figures 2.4c and 2.4d are SEM images of the SWCNT suspended between two micro-pillars and bird view of some pillar structures, respectively. Silicon was deposited on quartz substrate except the top of pillars so that growth of excess SWCNTs at the foot of pillars was suppressed; SWCNTs were not grown on silicon because of the silicidation of deposited cobalt. As shown in Fig. 2.4c, not only the suspended SWCNT but also SWCNTs on the pillar wall grew possibly due to the lack of silicon deposition on this side of the pillar wall.

## 2.2 Optical Measurement Setup

### Configuration

The home-made optical measurement setup based on the inverted optical microscope was employed for PL and Raman measurements. Figure 2.5 shows schematics of the optical measurement setup. Main light source was supplied by the pump laser generating laser light with the emission wavelength of 532 nm (Verdi V5, Coherent, United States), and then the wavelength of the light was tuned by the Ti:sapphire laser system (890 Ti:S DW-HN, Coherent, United States) from 700-840 nm. The wavelength of the incident laser light for Raman spectroscopy was fixed because the band pass filter centered at 785 nm in wavelength was set after the Ti:sapphire laser system so that well-defined wavelength of incident laser light was obtained. The intensity of laser light was then measured by the power meter. The intensity at the sample stage was calibrated beforehand and controlled with

changing the pump laser power and neutral density (ND) filters. The low pass filter was set on the laser line so that high order harmonic elements emitted from the Ti:sapphire laser system were cut. The laser light was then reflected by the dichroic mirror located below the objective lens in the inverted optical microscope. The dichroic mirror reflects light with wavelength shorter than approximately 950 nm, and passed through the others. The objective lens with fifteen-powered magnification and numerical aperture of 0.65 (LCPLN-50XIR, Olympus, Japan) were employed. The objective lens converged laser light on a spot with the diameter of approximately 1.6  $\mu\text{m}$ .

Photoluminescence with wavelength over 950 nm was corrected by the objective lens and went through the dichroic mirror while Raman scattering ranging from 785 nm to approximately 950 nm was reflected there. Two different detecting systems were used for PL detection. One is the conventional InGaAs detector array (OMA V InGaAs photodiode array 1024 channel, Princeton Instruments, United States) coupled with the spectrometer (ACTON Spectra Pro 2300i, Princeton Instruments, United States) for PL spectroscopy. The InGaAs detector array was cooled by liquid nitrogen to  $-100^{\circ}\text{C}$ . Photoluminescence ranging from 950 to 1600 nm in wavelength was measured by the detection system. For highly luminescent suspended SWCNTs with suspend length longer than the spot size of incident laser light, acquisition time on the order of  $10^0$ - $10^1$  seconds was employed and PL intensity over ten thousand counts was obtained. Although the clear confirmation is still lacking, quantum yields of approximately 7% was proposed for suspended SWCNTs [46]. On the other hand, acquisition time on the order of  $10^1$ - $10^2$  seconds was employed for suspended SWCNTs with shortly suspended length because the shorter SWCNTs generally shows the low PL intensity. PL intensity less than ten thousand counts was obtained for such shortly suspended SWCNTs. The wavelength resolution for PL spectroscopy was 0.5 nm, and wavelength of PL spectra were calibrated by emission spectra of mercury vapor. The other PL detection system was PL 2D imaging system based on the 2D InGaAs diode array detector coupled with the acoust-optic tunable filter (AOTF). The wavelength of incident light to the 2D InGaAs diode array detector was tuned by AOTF. The wavelength resolution of the AOTF was rough compared to the detection system used for PL spectroscopy. Although the center wavelength of PL detected by the 2D InGaAs diode array was controlled by the AOTF for every 1 nm steps, actual wavelength resolution was 20-50 nm depending on the center wavelength.

Raman scattering light reflected by the dichroic mirror went through the notch filter and Rayleigh scattering element was cut there. The spectrometer employed for Raman spectroscopy was the same product as that for PL spectroscopy but a high resolution grating was used. The air cooled CCD array detector (Pixis 100BR CCD array 512 channel, Princeton Instrument, United State) was used for the detection. The wavelength resolution for Raman spectroscopy was 0.1 nm. The acquisition time for Raman spectroscopy was on the order of  $10^1$ - $10^2$  seconds for highly luminescent SWCNTs. The wavelength of acquired Raman scattering light was calibrated by emission spectra of argon gas and mercury vapor.

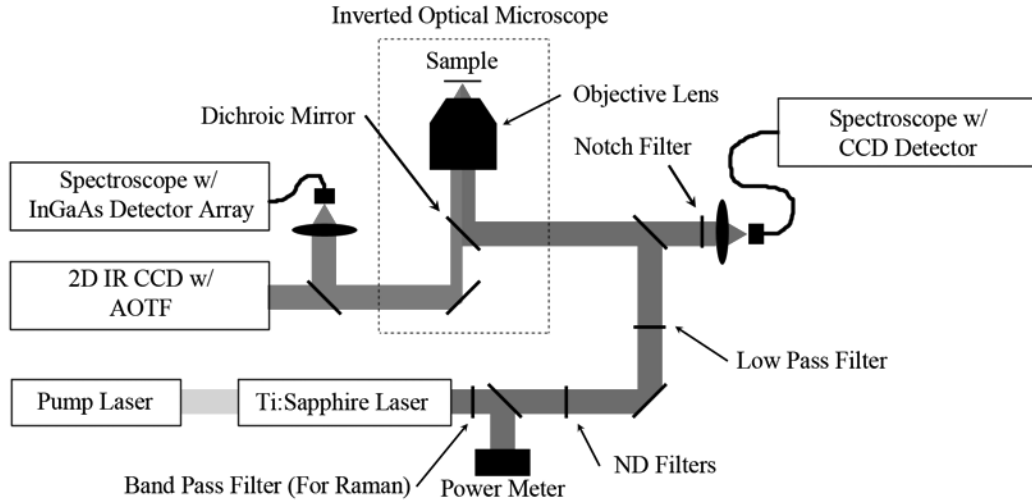


Fig. 2.5 Schematic drawing of the homemade optical measurement setup used for experiments.

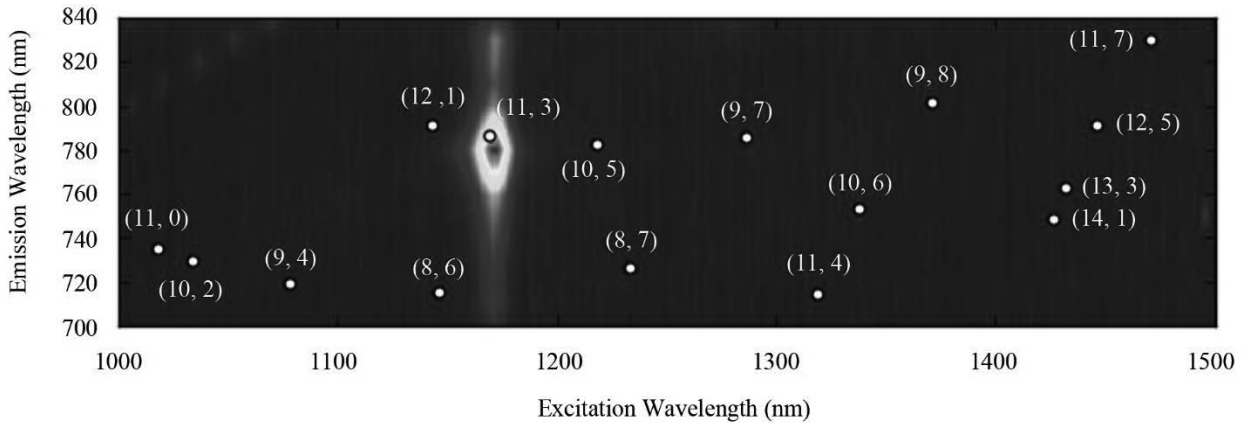


Fig. 2.6 Photoluminescence excitation map from the singly suspended (11,3) nanotube.

### Photoluminescence Excitation Map

The chirality of a suspended SWCNT was assigned from PL excitation map (PLE map) where  $E_{22}$  and  $E_{11}$  energies of suspended SWCNTs were measured. The wavelength of incident laser light was scanned by every 10 nm steps with keeping PL acquisition synchronized. Figure 2.6 shows a typical PLE map obtained from the singly suspended (11,3) nanotube that has  $E_{22}$  energy of 1.59 eV and  $E_{11}$  energy of 1.06 eV (corresponding to 780 nm and 1175 nm in wavelength, respectively). The single intensive peak on the image indicates successful growth of the suspended SWCNT without bundling. White circles and indices on the image indicate the expected peak position in air and corresponding chiral index for each chirality of SWCNTs [9]. Thus, 16 types of semiconductive SWCNTs were detectable by using the optical measurement setup above.

### 2.3 Generation of Atmospheric Ions

In experiments in chapter 4, the reaction between atmospheric ions and SWCNTs is discussed. Atmospheric ions were generated by the hand sized air ionizer (BF-SZAI, Shishido Electrostatic LTD., Japan) that is generally used for the removal of surface charges on a substrate. In the air ionizer

employed, four needle electrodes pointed radial direction while the plane electrode rolled up into a circle with the diameter of approximately 8 cm was placed around needle electrodes making a point-to-plane configuration. The alternating voltage of 2 kV was applied to those electrodes. Stable corona discharge was observed at the each tip of four needle electrodes when the ionizer was turned on. The small fan was placed at the back of those electrode supplying air flow to those electrodes. Air sent to those electrodes was ionized by corona discharge. Ionized air, thus atmospheric ions, directly reached to a sample surface without any acceleration voltage. The amount of air flow was 0.2-0.3 m<sup>3</sup>/min. For the reaction between atmospheric ions and SWCNTs, the air ionizer was set 15 cm away from a substrate supporting SWCNTs.

Components of atmospheric ions in air are complex. Products of corona discharge, for example, vary depending on components in air, applied voltage, and electrode configuration. The generation of atmospheric ions by corona discharge is firstly classified by the polarity of needle electrodes. In the case where positive bias is applied to a needle electrode, positive corona discharge occurs while the other case is called negative corona discharge. In positive corona discharge, the stable generation of hydronium ion (H<sub>3</sub>O<sup>+</sup>) was confirmed when water presented in air at least 0.04 mol% [10]. Negative corona discharge is even more complex. Some ionic species such as HCN<sup>-</sup>, CO<sup>-</sup>, OH<sup>-</sup>, and NO<sub>x</sub><sup>-</sup> were observed [13] for negative corona discharge, and the relative abundance of those ionic species varied depending on discharge condition. Although not only those ionic species but also neutral chemical species such as ozone or other radical oxygen are possibly generated by corona discharge, the amount of those chemical species is small. For example, the ozone density below 0.04 ppm was observed for the air ionizer employed according to the manufacturer. Water molecules play an important role for the lifetime of atmospheric ions in air. Water molecules stick to atmospheric ions reducing Coulomb potential; lower Coulomb potential are expected for larger cluster with given charge. It is also known that hydrated atmospheric ions with three water molecules are metastable structure [11][12]. Such hydrated atmospheric ions are referred to as “atmospheric ions” in this thesis.

Atmospheric ions exist, though sparse, all the time in natural environment. The amount of atmospheric ions in natural environment is on the order of 10<sup>3</sup>/m<sup>3</sup> [14]. Those atmospheric ions in natural environment are generated by, for example, cosmic radiation, discharge in air, or splashing water. In this thesis, the amount of atmospheric ions generated by corona discharge were roughly estimated by using the commercial ion counter (NKMH-103, Hokuto Electronics Inc., Japan). Positive atmospheric ions with the density of 5.1 × 10<sup>10</sup>/m<sup>3</sup>, and negative atmospheric ions with the density of 3.6 × 10<sup>10</sup>/m<sup>3</sup> were observed at the position 15 cm away from electrodes. Note that the ion counter gives only rough estimation of generate ions. More precise measurements for the ion amount as well as the assignment of ionic species will give further insights into results obtained in this thesis.

## References

- [1] S. Maruyama, R. Kojima, Y. Miyauchi, S. Chiashi, M. Kohno, Chem. Phys. Lett. 360, 229 (2002)
- [2] H. Liu, D. Takagi, S. Chiashi, and Y. Homma, Nanotech. 20, 345604 (2009)

- [3] S. Suzuki, Y. Kobayashi, Chem. Phys. Lett. 430, 370 (2006)
- [4] Y. Homma, S. Suzuki, Y. Kobayashi, M. Nagase, and D. Takagi, Appl. Phys. Lett. 84, 1750 (2004)
- [5] L. Huang, X. Cui, B. White, and S. P. O'Brien, J. Phys. Chem. B 108, 16451 (2004)
- [6] J. Lefebvre, Y. Homma, and P. Finnie, Phys. Rev. Lett. 90, 217401 (2003)
- [7] T. Matsumoto, Y. Homma, and Y. Kobayashi, Jpn. J. Appl. Phys. 44, 7709 (2005)
- [8] J. Lefebvre, D. G. Austing, J. Bond, and P. Finnie, Nano Lett. 6m 1603 (2006)
- [9] J. Lefebvre, and P. Finnie, Phys. Rev. Lett. 98, 167406 (2007)
- [10] M. M. Shahin, J. Chem. Phys. 45, 2600 (1966)
- [11] Y. K. Lau, S. Ikuta, and P. Kebarle, J. Am. Chem. Soc. 104, 1462 (1982)
- [12] K. Sekimoto, and M. Takayama, Int. J. Mass Spectrom. 261, 38 (2007)
- [13] K. Sekimoto, and M. Takayama, Eur. Phys. J. D 50, 297 (2008)
- [14] A. Hirsikko, T. Nieminen, S. Gagne, H. E. Manninen, M. Ehn, U. Horrak, V.-M. Kerminen, L. Laakso, P. H. McMurry, A. Mirme, S. Mirme, T. Petaja, H. Tammet, V. Vakkari, M. Vana, and M. Kulmala, Atmos. Chem. Phys. 11, 767 (2011).

# Chapter 3

## Intrinsic Exciton Diffusion Length and Exciton-Exciton Annihilation

### 3.1 Introduction

In this chapter, evaluation of intrinsic diffusion length of excitons in a long suspended SWCNT is shown by analyzing the length dependence of PL emission intensity. The PL emission intensities depending on the tube length are all obtained from one individual long SWCNT suspended on a groove patterned substrate. The exciton dynamics is described by a 1D diffusion equation. The diffusion length in the clean and pristine long SWCNTs is found to be constant, about 200 nm at a lower laser power regime, indicating an intrinsic diffusion behavior. From the intrinsic diffusion length obtained, the threshold laser power of  $10^{21}$  photons/cm<sup>2</sup>·s, which is consistent with the onset of exciton-exciton annihilation, was estimated.

Optical processes in SWCNTs are dominated by the dynamics of excitons which are confined in 1D structure of SWCNTs with a large binding energy on the order of several hundred meV [1][2]. Excitons are diffusive in nature in SWCNTs [3], and exciton mobility is one of the fundamental properties for understanding the optical responses of SWCNTs. In a diffusion model, exciton motion is characterized by diffusion length ( $L$ ). All diffusing excitons move in a way proportional to  $\sqrt{D\tau}$ , independent of dimensionality. Here,  $D$  and  $\tau$  are the diffusion coefficient and lifetime, respectively. Up to now, many experimental studies have been carried out to investigate the exciton diffusion length in semiconducting SWCNTs but leaving largely scattered values. It differs by several orders of magnitude, ranging from  $10^0$  to  $10^2$  nm [3]-[8]. Most of those measurements were performed on surfactant- or DNA-wrapped SWCNTs, representing averaged results and preventing a detailed spectral analysis. Discrepancy among the experimental results has not yet been clarified. On the other hand, it is expected that the transport properties of excitons are extremely sensitive to their surroundings. Exciton diffusion length depends on the type of surfactant, and is positively correlating to PL intensity [6]. Furthermore, exciton motion is strongly affected by trapping states and laser power [7][8]. Therefore, fabrications of well-separated SWCNTs with a high quality are essential for investigating their intrinsic electronic and optical properties. It is also believed that the intrinsic diffusion length of the excitons in SWCNTs is of essential importance for understanding the basic physics and future applications. For example, the intrinsic diffusion length relates to single-exciton SWCNT device applications such as single photon emitter because the design of device size is determined by the diffusion length for prohibiting the EEA. Excitons move a significant distance before recombination in SWCNTs transporting energy from one point to another. Deep

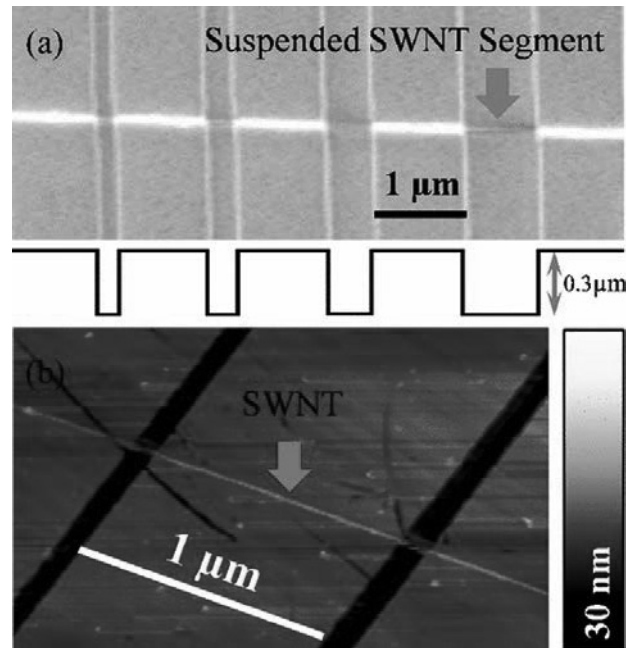


Fig. 3.1 (a) Top: An SEM image of a long suspended SWCNT on groove patterned quartz substrate with diverse groove widths. Bottom: Schematic cross section of the groove patterned substrate. (b) A typical AFM image of a long suspended SWCNT on two grooves. Reprinted with permission from [30]

understandings of exciton motion in SWCNTs may also open up a possibility for the improvement of collection or energy transfer in light harvesting devices based on SWCNTs.

In this chapter, the intrinsic diffusion length of excitons in a long suspended SWCNT is studied. The length dependence of PL intensities from an SWCNT was used to evaluate the diffusion length, and more importantly, the dependence of PL intensity on tube length was obtained from the same long suspended SWCNT on the groove patterned substrate. The result of experiment shows that the exciton diffusion length in freely suspended SWCNTs can be as large as 200 nm. The laser power independence of diffusion length in a lower excitation regime shows an intrinsic diffusion nature of excitons, which has not been clearly recognized in the previous papers [3]-[8]. Additionally, the onset laser power where the EEA begins to significantly affect the diffusion length is also analyzed.

## 3.2 Experiments

SWCNTs were prepared on a well-designed groove patterned quartz crystal substrate by a gas flow method in alcohol chemical vapor deposition [9]. The groove width on the substrates varied from 200 to 800 nm periodically with a depth of about 300 nm fabricated by the photolithography method (Fig. 3.1a). Iron catalyst for SWCNT growth was deposited by the vacuum deposition. The catalyst deposited substrate and patterned substrate were separated as shown in Fig. 2.3. Long SWCNTs

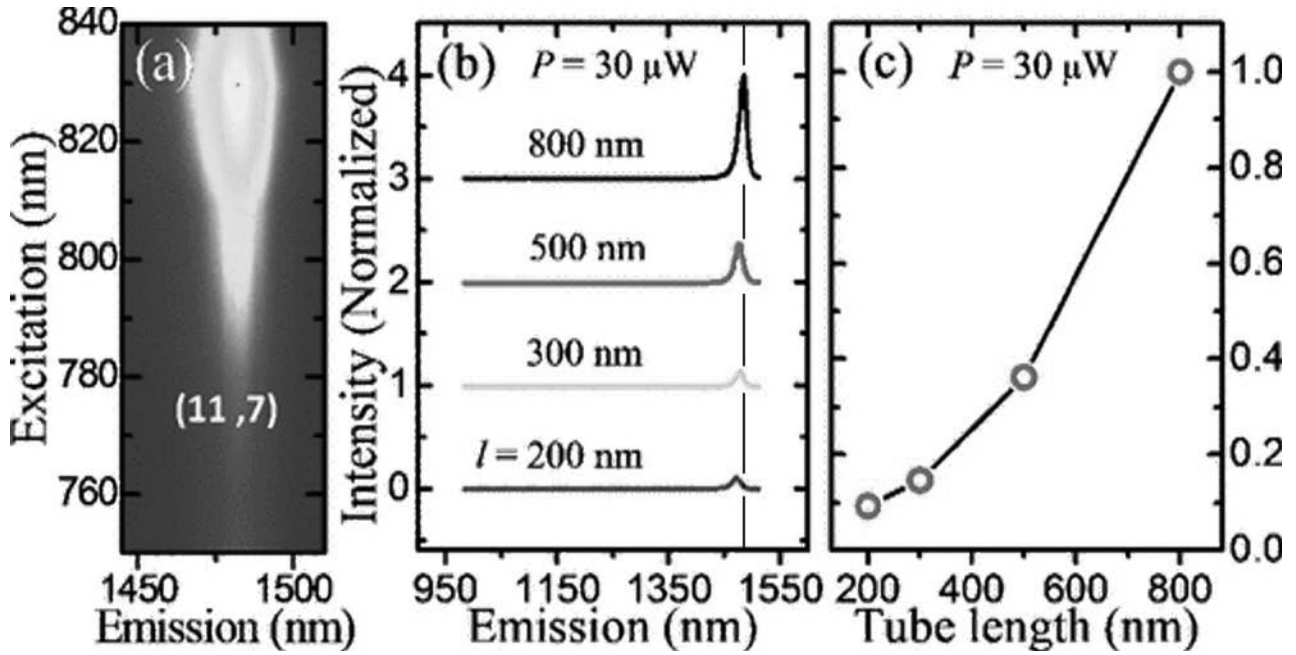


Fig. 3.2 (a) Photoluminescence excitation map of the studied suspended SWCNT. The SWCNT can be assigned to a chirality of (11, 7) with a diameter of 1.2 nm. (b) Emission spectra (normalized intensity) from diverse tube segments at excitation power of  $30 \mu\text{W}$ . The spectra are shifted for clarity. (c) Photoluminescence intensity as a function of tube length corresponding to (b). The solid line is a guide to the eye. Reprinted with permission from [30]

grown on the catalyst deposited substrate and extended to the receiving patterned substrate by gas flow. Long SWCNTs suspended perpendicularly to the direction of the grooves. The SEM image of typical long SWCNT sample is shown in Fig. 3.1a. Figure 3.1b shows the AFM image of a long suspended SWCNT on two typical grooves. Both of the SEM and AFM images demonstrate the successful synthesis of nicely suspended SWCNTs. For the PL measurements, the polarization of the excitation laser is set to be parallel to the z axis of the SWCNTs so that the excitation laser is effectively absorbed by the SWCNTs [25]. Semiconducting SWCNTs that had intense and sharp emission peaks with narrow FWHM, which were thought to be high-quality SWCNTs with few defects, were carefully chosen in advance for the experiments. SWCNTs are non-luminescent on silica, thus unsuspended segments, due to the significant substrate-induced non radiative decay of excitons [11]. Therefore, we here assumed a perfect quencher at the edge of suspended segments, and only the suspended segments contributed to SWCNT PL.

### 3.3 Length Dependence of Photoluminescence Intensity

The studied SWCNT was first identified by a PLE map where the  $E_{11}$  and  $E_{22}$  transition energies were determined [12]. A typical PL excitation map performed on a suspended segment, 800 nm long, is shown in Fig. 3.2a. The resonant excitation and emission wavelengths were found at 830 nm and 1483 nm, respectively. Those are consistent with the chirality of (11, 7) with a diameter of 1.2 nm,

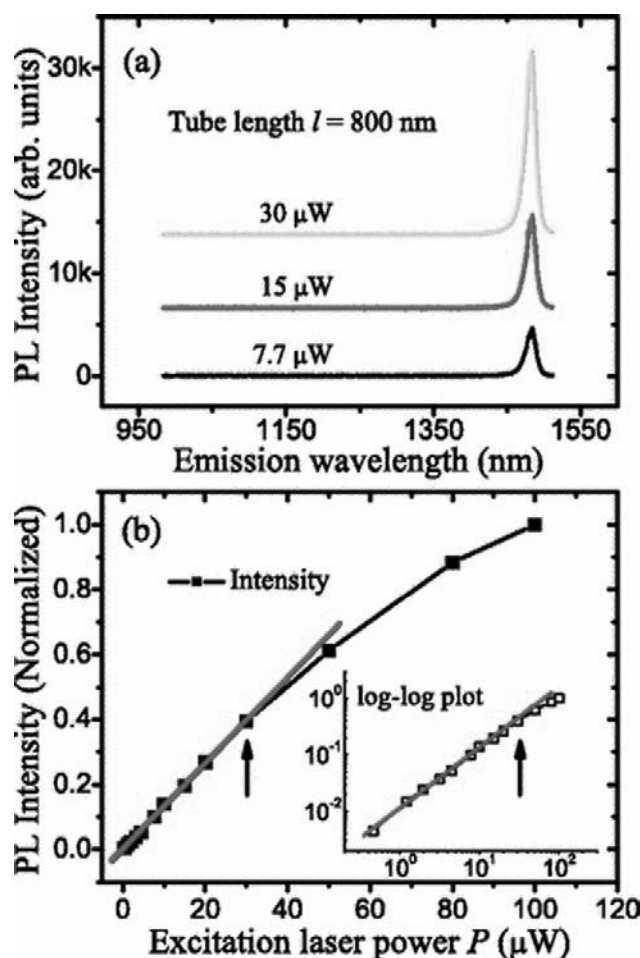


Fig. 3.3 (a) Nanotube emission spectra at excitation powers of 7.7 (black), 15 (red), and 30  $\mu\text{W}$  (green) for tube length  $l = 800$  nm. The spectra are shifted for clarity. (b) Excitation laser power dependence of photoluminescence intensity. Inset shows a log-log plot. The linear fittings at lower power regime are shown by the solid red lines. Black arrows indicate the onset laser power (30  $\mu\text{W}$ ) for nonlinearity. Reprinted with permission from [30]

considering the wavelength shift for air-suspended SWCNTs [12]-[14]. However, we should note that small blue shifts of excitation and emission wavelengths were observed for shorter nanotube segments as shown in Fig. 3.2b. The origin of the small blue shifts will be discussed later.

Subsequently, the dependence of PL intensities on tube length was obtained by resonantly exciting ( $\lambda = 830$  nm) the different suspended segments from the same SWCNT. Figure 3.2b shows the measured emission spectra at excitation laser power ( $P$ ) of 30  $\mu\text{W}$  for tube length varying from 200 to 800 nm. The PL intensities increase with tube length as shown in Fig. 3.2c. Here, the time traces of PL intensity were also performed to check the PL stability, and no spectral shifts, broadening, or change in the emission intensity during the experimental duration were observed.

Because of the larger laser spot size, with increasing of  $l$ , we did not observe any saturation of

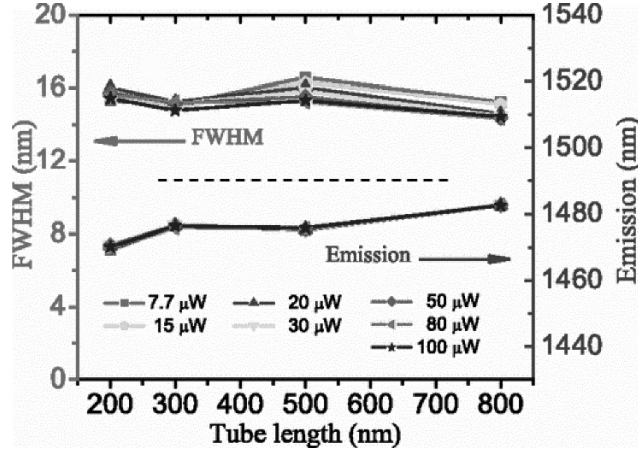


Fig. 3.4 Emission wavelength (bottom) and FWHM (upper) of photoluminescence emission peak as a function of tube length under different excitation laser powers. Reprinted with permission from [30]

PL intensity with  $l \geq 800$  nm. However, it is expected that PL intensity will finally saturate when  $l$  is enough larger than the laser spot size and excitons generated in the SWCNT recombine before reaching unsuspended segments. In that case, most of the excitons recombine before they diffuse to the unsuspended segments, and after that,  $l$  does not play a role for the PL intensity [7].

Additionally, for each fixed suspended tube segment of the SWCNT, we collected a series of PL spectra as a function of laser power. Figure 3.3a shows three typical emission spectra with excitation laser power of 7.7, 15, and 30  $\mu\text{W}$  for  $l = 800$  nm. As depicted in Fig. 3.3b, it is found that PL intensity rises as excitation laser power increases. It scales linearly with  $P$  in the lower power regime. However, it deviates from the linearity at a higher power. The inset is the log-log plot of the main graph of Fig. 3.3b. The solid red straight lines are the linear fittings in the lower power regime. The black arrows in both the inset and main graphs indicate the onset power where the nonlinearity occurs. The onset power can be read approximately 30  $\mu\text{W}$  corresponding to a photon fluence of about  $10^{21}$  photons/cm<sup>2</sup>·s. The nonlinear behavior is attributed to the EEA effect [15]-[17]. Generally, the larger laser power induces the larger number of excitons; correspondingly, there is a higher probability for EEA. If the EEA process is efficient, it will quickly deplete the population of excitons, resulting in the PL intensity reduction. The annihilation of the excitons is reduced when a small number of excitons are excited.

Although PL is stable for fixed suspended segments, small variations of the emission wavelength as well as the FWHM of the spectra line were observed from different suspended segments under various laser power as shown in Fig. 3.4. For instance, at  $P = 30 \mu\text{W}$ , the measured standard deviations of the emission wavelength and spectral FWHM from  $l = 200$  to 800 nm are 4.2 and 0.5 nm, respectively. The variations of the emission wavelength with tube length may be attributed to the strain imposed from the unsuspended segments, because the nanotubes are distorted

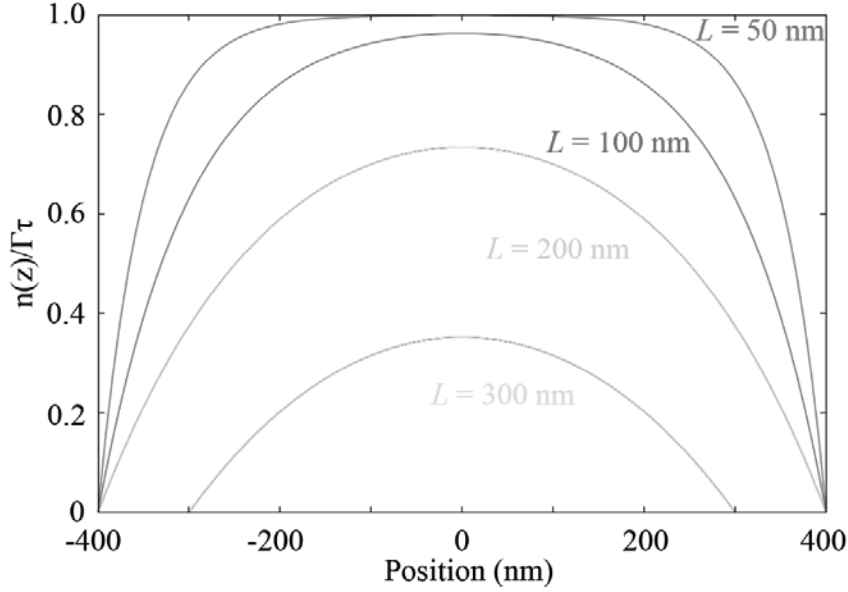


Fig. 3.5 Exciton density  $n(z)/\Gamma\tau$  for various diffusion length  $L$ . The nanotube length  $l$  was set to 800 nm.

by the interaction with the substrate surface [18]. Strain can be created on the suspended segments, which can cause the shift of vHs [19], and a large effect is expected for a short suspended segment.

### 3.4 Intrinsic Diffusion Length of Exciton in Single-Walled Carbon Nanotubes

Photoluminescence originates from the recombination of excitons; hence, the PL intensity is determined by the total number of excitons in SWCNTs. For understanding the exciton movement in SWCNTs with microscopic viewpoint, one need to formulate the equation of motion for exciton distribution together with the consideration of interaction with electron and hole. This is corresponding to formulate Boltzmann equation for exciton distribution. However, the formulation of such equation is generally complicated and it is also difficult to solve the equation. On the other hand, simplification with which the equation of movement for averaged exciton density is treated instead of exciton distribution is often employed [6][7]. Here, the exciton dynamics in SWCNTs can be described with the 1D diffusion equation. Note that diffusion constant  $D$  cannot be determined with first principle approach because of the simplification but fitted to experimental data. The exciton density  $n(z)$  which determines the PL intensity varies along the suspended SWCNT segments. The  $n(z)$  is expected to decrease from the groove center to both edges. In order to obtain the intrinsic diffusion length from the dependence of the PL intensity on nanotube length  $l$ , the exciton density profile based on a steady-state 1D diffusion equation is firstly derived.

$$D \frac{d^2 n(z)}{dz^2} - \frac{n(z)}{\tau} + \Gamma(z) = 0 \quad (3.1)$$

The first term accounts for the exciton diffusion. The second term describes the decay process and  $\tau$  is an intrinsic lifetime of excitons typically on the order of  $10^2$  ps [16][23]. The last term  $\Gamma(z)$  is the

exciton generation rate. Here, homogeneous generation of exciton  $\Gamma(z) = \Gamma$  is assumed because spot size of excitation laser light is larger than the suspended segments. Based on the boundary condition where  $n(z)$  goes zero at both edges ( $z = \pm l/2$ ) of the suspended SWCNT, Eq. 3.1 can be solved to;

$$n(z) = \Gamma\tau[1 - \cosh(\frac{z}{L})\cosh^{-1}(\frac{l}{2L})] \quad (3.2)$$

Here, boundary condition employed is consistent with the experimental fact that the PL intensity of suspended SWCNT decays near edges of suspended segment and almost no PL can be observed at those edges. The exciton density  $n(z)/\Gamma\tau$  is plotted in Fig. 3.5 as a function of position  $z$  for various diffusion length  $L$ . The nanotube length  $l$  was set to 800 nm in Fig. 3.5. Consequently, the entire PL intensity  $I$  from a certain segment can be obtained by integrating the exciton density profile;

$$I = \int_{-l/2}^{l/2} n(z)dz = \Gamma\tau[l - 2L\tanh(\frac{l}{2L})] \quad (3.3)$$

The derived PL intensity for a range of nanotube lengths  $l$  and a series of diffusion lengths  $L = \sqrt{D\tau}$  are plotted in Fig. 3.6a. The PL intensity goes up quickly with  $l$  for shorter  $L$ . Photoluminescence intensity scales linearly with tube length when  $L$  equals zero as shown with the blue line in Fig. 3.6a. On the other hand, for a fixed  $l$ , larger  $L$  results in a relatively lower PL intensity, which indicates an inefficient recombination of exciton caused by diffusion process. As the  $L$  gets longer, excitons more easily diffuse to the edges of suspended segments leading to significant substrate-induced non-radiative decay.

The experimental data for  $l$  dependence of PL intensity was fitted to Eq. 3.3 under each excitation laser power to extract  $L$ . All of the PL intensity from the spectra, which were collected for 180 s under a high signal to noise ratio, were read by the area under a Lorentzian fitting curve. During data fitting, a parameter was inserted in Eq. 3.3 to describe the background signal. A constant offset of the fitting lines is found, which is probably attributed to the constant background signal of the PL measurement system. For a fixed excitation laser power, the value of  $\Gamma\tau$  is counted as a constant; hence, the PL intensity is only a function of tube length and diffusion length. Figures 3.6b to 3.6d show the measured PL intensity as a function of tube length at  $P = 20, 30,$  and  $50 \mu\text{W}$ , respectively. The solid lines represent the best fits, which give  $L = 221, 220,$  and  $168\text{nm}$  for Figs. 3.6b to 3.6d. The variability of data is estimated by the error bar in all graphs, and the relative error was 10-20%.

The diffusion length was plotted as a function of laser power in Fig. 3.7a. For the lower laser power,  $P \leq 30 \mu\text{W}$ , the diffusion length scatters from 188-237 nm. However, there is no obvious laser power dependence, and the average value is 219 nm as shown with the solid red line in Fig. 3.7a. The lower laser power corresponds to a lower exciton density where the EEA is negligible. Hence, the diffusion length in the lower power regime is expected to be the intrinsic diffusion length of excitons in SWCNTs, which means excitons diffuse a significant distance within their intrinsic life time before their recombination. The exciton diffusion lengths previously reported in the surfactant-

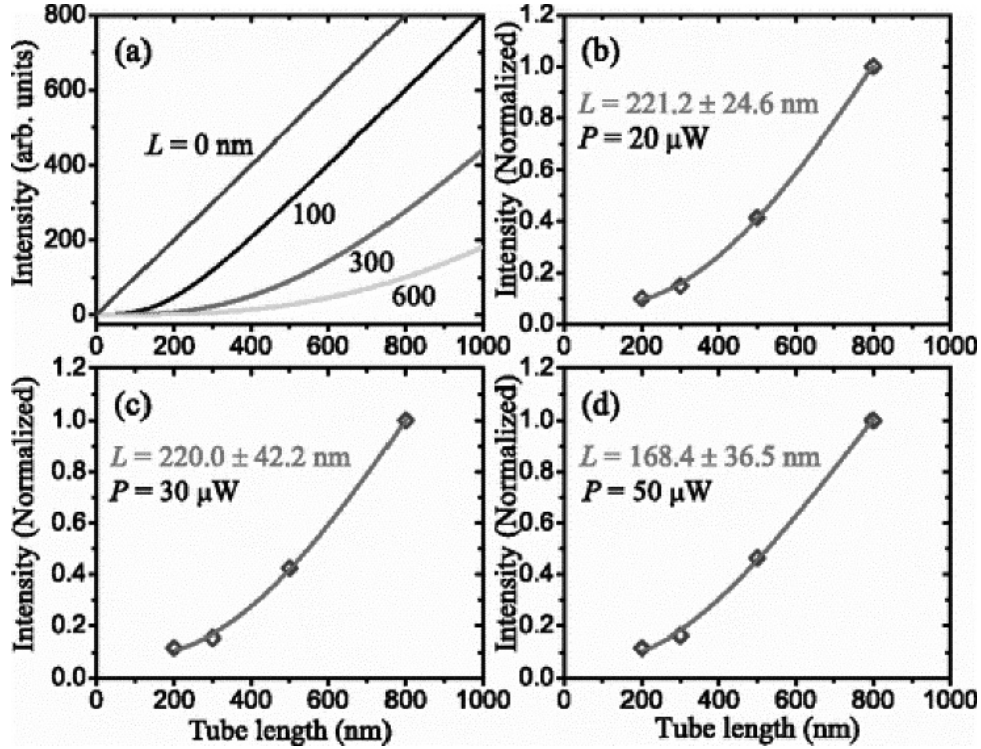


Fig. 3.6 (a) Simulated PL intensity as a function of tube length for diffusion length  $L = 0$  (blue), 100 (black), 300 (red), and 600 nm (green), respectively. (b-d) show the measured PL intensity as a function of tube length for laser power  $P = 20, 30,$  and  $50 \mu\text{W}$ , respectively. The solid red lines represent the data fittings. Reprinted with permission from [30]

or DNA-wrapped SWCNT samples are shorter than those evaluated from long suspended SWCNT [3]-[6]. This is probably due to the surfactant related non-radiative recombination of excitons in those samples [20]. The generation of new decay paths for excitons reduces the total lifetime  $\tau$  and thus the diffusion length defined as  $L = \sqrt{D\tau}$  decreases. Similar  $L$  values have been reported for other air-suspended SWCNTs, about  $\sqrt{2}L = 200 \text{ nm}$  by PL imaging [8], and  $L = 280 - 680 \text{ nm}$  by length dependent PL from different tubes [7]. For the latter, although the effects of EEA was not discussed, the results showed an obvious laser power dependence due to the EEA effect. Furthermore, the existence of tube to tube variations also increase the scattering of the data.

### 3.5 Onset Power for Exciton-Exciton Annihilation; Analysis of Experimental Results

For  $P > 30 \mu\text{W}$ , the power dependent decay behavior of  $L$  has been observed as presented in Fig. 3.7a in the large power regime. One can conclude that the onset power is consistent with that of EEA in SWCNT. Excitons can be rather efficiently eliminated at high densities through the EEA process which is in agreement with previous claims [15][21]. This would explain the deviation of PL intensity and exciton diffusion length from those linear fitting lines at low power regime with increasing laser power as shown in Fig. 3.3b and Fig. 3.7a, respectively. The lifetimes of excitons is regarded to be

reduced due to EEA [3]. For a higher laser power, the excitons only diffuse a mean-free path before the annihilation or recombination occurs due to EEA, and finally, the mean-free path is expected to be determined by a maximum density.

In the main graph of Fig. 3.7b, we plotted  $\Gamma\tau$  as a function of laser power after data fitting.  $\Gamma\tau$  is found to be proportional to  $P$  at the lower power regime meaning linear dependence of  $\Gamma$  on  $P$ . while for  $P$  larger than  $30 \mu\text{W}$ ,  $\Gamma\tau$  begins to deviate from the linear behavior. The onset laser power is consistent with those in the PL intensity and diffusion length cases shown in Fig. 3.3b and Fig. 3.7a. We assume that, for the first-order approximation, at the lower laser power regime with a lower exciton density where EEA effect is negligible,  $\tau$  is constant indicating an intrinsic lifetime of excitons, and also  $\Gamma$  is proportional to  $P$ , i.e.,  $\Gamma = A_0P$  with  $A_0$  as the proportional constant. Consequently,  $\Gamma\tau$  scales linearly with  $P$ ,  $\Gamma\tau = A_0\tau P$ , as shown in the main graph of Fig. 3.7b (linear part). The value of

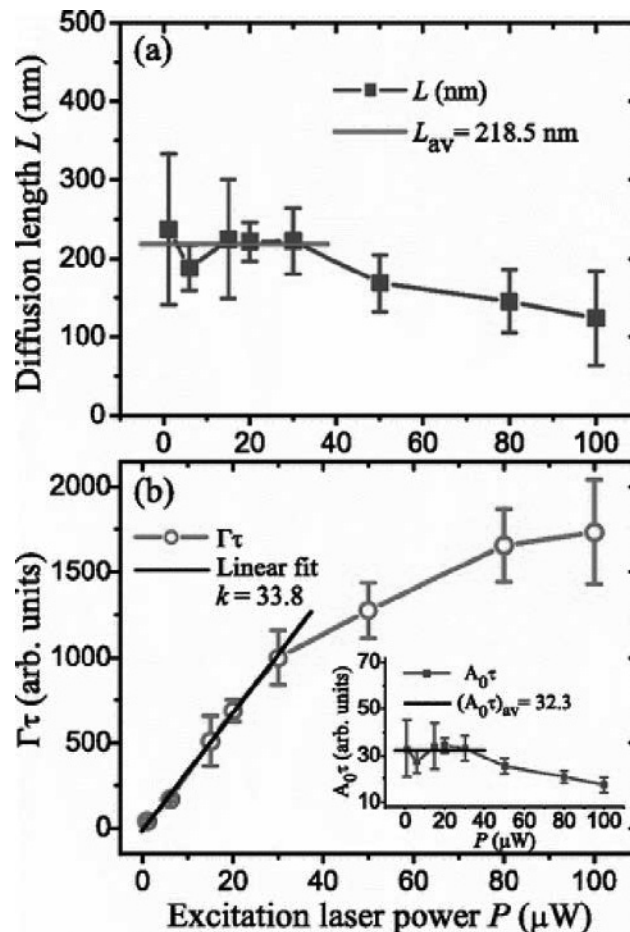


Fig. 3.7 (a) Excitation laser power dependence of exciton diffusion length. The solid red line indicates the average value of diffusion length in the low-power regime. The reduction of the diffusion length in the high-laser-power regime is due to the EEA effect. (b)  $\Gamma\tau$  as a function of laser power. The solid black line shows the linear fitting in the low-power regime.  $A_0\tau$  as a function of laser power is shown in the inset. The solid black line gives the average value of  $A_0\tau$  in the low-power regime. Reprinted with permission from [30]

$A_0\tau$  relating to the exciton lifetime is given by the slope  $k$  from the linear fitting (solid black line with  $k = 33.8$ ). On the other hand,  $A_0\tau$  as a function of  $P$  shown by the inset can be deduced from the main graph of Fig. 3.7b, i.e.,  $A_0\tau = \Gamma\tau/P$ . The scaling behavior of  $A_0\tau$  is analogous to the diffusion-length case. For  $P \leq 30 \mu\text{W}$ , the  $A_0\tau$  is approximately a constant value (32.3 on average) presented by solid black line in the inset. For higher  $P$ ,  $A_0\tau$  decaying quickly with laser power again provides evidence for the onset of the EEA effect in SWCNTs. The reduction of the exciton lifetime in the high power regime may be responsible for the decrease of diffusion length (see Fig. 3.7a and the inset of Fig. 3.7b). The laser power independence for both  $L$  and  $\tau$  in the lower power regime allow us to conclude

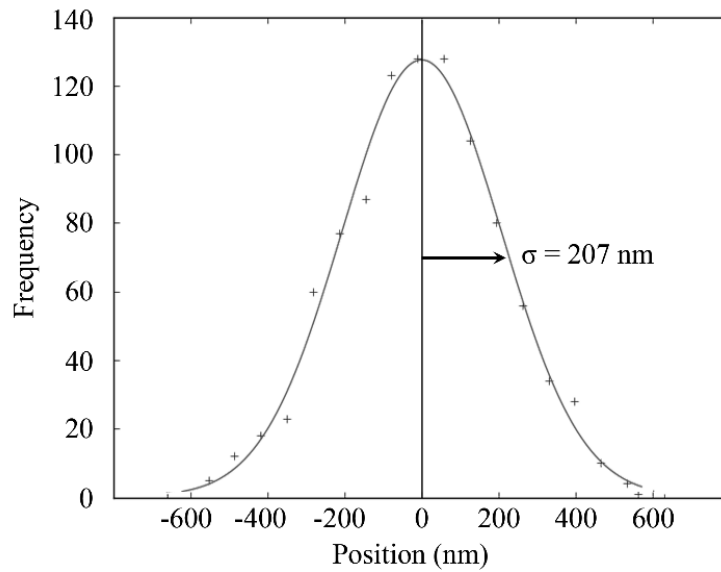


Fig. 3.8 Histogram of positions where each one of 1000 excitons shows radiative decay without the consideration of EEA.

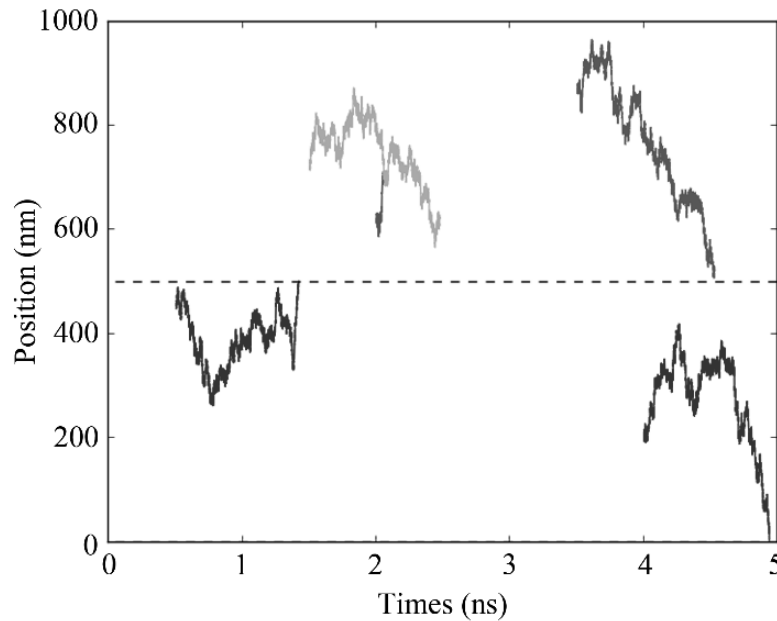


Fig. 3.9 Time trace of excitons diffusing in a 1000 nm long SWCNT with quench point located at the center of the SWCNT.

that exciton shows an intrinsic diffusion behavior.  $L$  and  $\tau$  can be regarded as the intrinsic diffusion length and lifetime in this regime, respectively.

Analysis of the PL intensity, exciton diffusion length, and life time depending on laser power enables us to identify the threshold laser power of approximately 30  $\mu\text{W}$  with the wavelength of 830 nm, which is corresponding to  $10^{21}$  photons/ $\text{cm}^2\cdot\text{s}$  and consistent with the onset of EEA for suspended SWCNTs. Most previous works reported the onset of sub-linearity at much higher excited laser power [15][16][20]. Moreover, there exists an upper limit to the exciton density in SWCNTs caused by the EEA [15][16]. The laser power for the PL saturation observed for long suspended SWCNT sample is 1.0 mW corresponding to an excitation photon fluence of  $10^{23}$  photons/ $\text{cm}^2\cdot\text{s}$  which is much lower than the values reported in Ref. 22 and 15 for encapsulated SWCNTs with a pump fluence of about  $10^{26}$  photons/ $\text{cm}^2\cdot\text{s}$ . Furthermore, the obtained photon fluence of  $10^{23}$  photons/ $\text{cm}^2\cdot\text{s}$  is one order of magnitude lower than that measured in Ref. 16 for long suspended SWCNTs with a pump fluence of about  $10^{24}$  photons/ $\text{cm}^2\cdot\text{s}$ . The larger diffusion length and life time in a long suspended SWCNT may account for the lower EEA threshold because the EEA threshold is inversely proportional to  $L$  and  $\tau$ . Under  $P = 30 \mu\text{W}$ , the exciton density is estimated to be about 1 in a 200-nm-long segment with  $\tau$  on the order of  $10^2$  ps [16][23] and the assumption that the quantum efficiency is about 7% [24]. The onset of EEA occurring at a low exciton density calls for new consideration of the nature of exciton interactions in aquasi-1D system [16].

### 3.6 Onset Power for Exciton-Exciton Annihilation; Numerical Simulations

Finally, in order to verify the onset power for EEA, 1D Monte Carlo simulation for exciton diffusion in an SWCNT were carried out. Details of the simulation are shown in appendix. Here, logic employed for the simulation is briefly introduced. The goal of this simulation is reproducing experimental result shown in Fig. 3.3b, the saturation behavior on PL intensity versus excitation intensity plot, by Monte Carlo simulation for exciton diffusion with EEA. In addition to the excitation intensity dependence, the visualization of implicit physical values such as the number of excitons that show EEA as a function of excitation intensity were also subjects of the simulation.

Diffusion length of excitons is one of the important parameter for the Monte Carlo simulation of exciton diffusion. The speed of excitons for every step in the simulation was determined so that the diffusion length was equal to the intrinsic diffusion length derived above. Figure 3.8 shows the histogram of positions where each one of 1000 excitons showed radiative decay. Here, all excitons were generated at the center of the 1D axis. Each one of excitons then diffused along the 1D axis of the SWCNT until the fixed radiative decay lifetime of 1 ns [25]. EEA was not considered in Fig. 3.8. The histogram was well fitted by a Gaussian distribution function (solid line) with standard deviation of 207 nm corresponding to the intrinsic diffusion length.

Figure 3.9 is one of the result showing the time trace of 5 excitons diffusing in a 1000 nm long SWCNT with quench point located at the center of the SWCNT. Three decay paths were considered for diffusing excitons in the following simulation. First one was radiative decay in which an exciton

survives until radiative decay lifetime of 1 ns [25] and then annihilated with emitting a photon. The others were non-radiative decay paths due to quench points and EEA. The dotted line at 500 nm in Fig. 3.9 represents the position of such a quench point. First generated exciton quenched at the point. Although a quench point was set at the center of the 1D axis in Fig. 3.9 for the easiness of understanding, quench points were basically set only at both edge of the SWCNTs in the following simulation. Second generated exciton survived for its radiative decay time, while third generated exciton quenched by EEA process with second one. As shown in Fig. 3.9, excitons were generated as time goes. This is different from Monte Carlo simulation in past researches where all of excitons were generated at the beginning of the simulation [26][27]. Continuous generation of exciton in the simulation corresponds to the PL experiments using the CW laser system as shown in the experiment above. Exciton generation rate was converted into CW laser power with 785 nm in wavelength. Absorption cross section of  $5 \times 10^{-17} \text{ cm}^2/\text{carbon}$  [28][29] for carbon atoms in an SWCNT and Gaussian laser profile with the standard deviation of 800 nm were considered for the conversion.

Figure 3.10a and 3.10b show frequencies of each recombination paths for excitons diffusing in

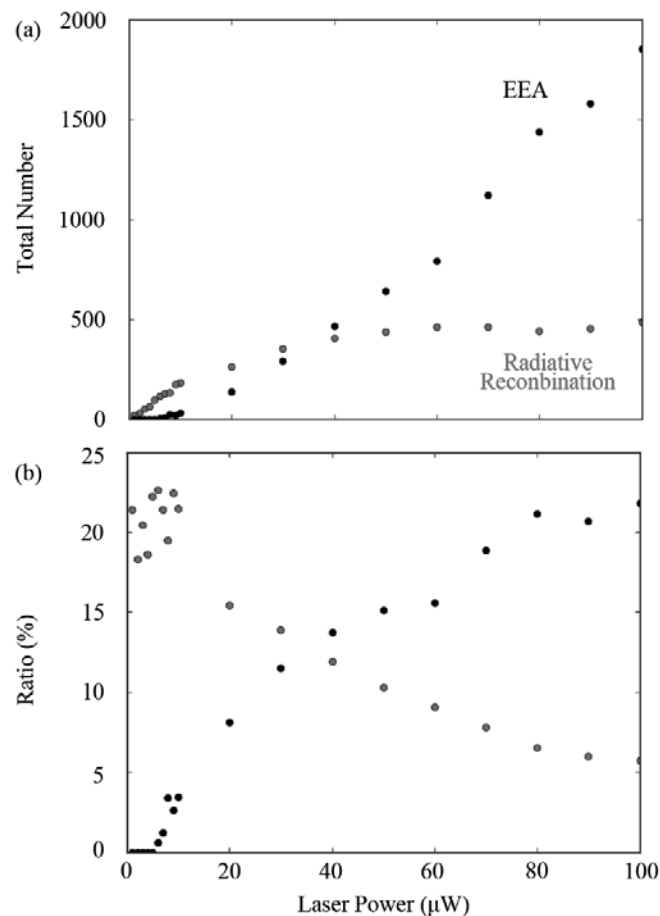


Fig. 3.10 (a) Frequencies of recombination paths, radiative recombination and EEA, for excitons diffusing in in 800 nm long SWCNTs and (b) corresponding ratios.

800 nm long SWCNTs and corresponding rates as a function of laser power. Total number of exciton generated in simulation time of 500 ns varies depending on the laser power. For example,  $8.5 \times 10^3$  excitons were generated at the laser power of 100  $\mu$ W. Because of shorter length of SWCNTs compared to laser spot, almost 80% of excitons generated decay due to quench point located at edges of the SWCNT which can be regarded as the significant substrate-induced non-radiative decay of excitons in actual experiments [11]. Ratio of radiative decay shown in Fig. 3.10b corresponds to external quantum yield of SWCNTs suspended on a groove with the width of 800 nm. Large scattering was observed on the ratio and will be discussed in appendix.

As shown in Fig. 3.10a, the total number of radiative decay well reproduced experimental results shown in Fig. 3.3b. The rate of EEA started to increase over 10  $\mu$ W. This value is small but consistent enough with the experimental value. The smaller onset power for EEA in the simulation is possibly due to the definition of laser spot and absorption cross section employed for the simulation. For example, the larger spot size of incident laser light in our experiment results in the smaller exciton generation rate in the 800 nm long SWCNT, thus the larger onset power for EEA in Fig. 3.3b. The smaller absorption cross section in our sample than published data [28][29] also results in the larger onset value for EEA in Fig. 3.3b. Ensemble SWCNTs immobilized on agarose gel were employed for the derivation of the absorption cross section in Refs 28 and 29. Quite a few SWCNTs were detected for such ensemble sample while only one SWCNT existed in laser spot in our sample. The difference in sample geometry is possibly responsible for the smaller absorption cross section in our experiments. On the other hand, non-radiative decay which was not clearly assumed in the simulation is not major factor for the difference between the simulation and the experiment because those effects were already included in the intrinsic diffusion length.

An upper value was observed for excitons showing radiative recombination in Fig. 3.10a. Figure 3.10a shows that only 400 excitons were able to exist in an 800 nm long SWCNT during the simulation time of 500 ns. The upper value suggests that 2 or more excitons hardly existed in an 800 nm long SWCNT at the same time. As a result, the rate of excitons showing radiative recombination was inversely proportional to the laser power at the high power regime. Therefore, intrinsic quantum yield can be obtained only with the low power regime, and such intrinsic quantum yield would be regulated by the abundance of non-radiative decay paths.

### 3.7 Summary

The SWCNT-sample structure grown by gas flow method was developed for evaluating the intrinsic diffusion length of excitons in a long suspended SWCNT by PL spectra. A freely suspended SWCNT is more ideal to study fine structures and intrinsic optical properties of excitons than surfactant wrapped SWCNT. The results showed that the intrinsic diffusion length of excitons in SWCNTs was as large as 200 nm for a long suspended SWCNT. Exciton-exciton annihilation is thought to be a possible mechanism to explain the reduction of diffusion length with increasing excitation laser power. An onset laser power to non-linearity of PL intensity consistent with EEA was found of  $10^{21}$

photons/cm<sup>2</sup>·s for a long suspended SWCNT. Further precise works on the exciton diffusion length evaluation from suspended SWCNTs should be performed on the same or several chiralities in vacuum or other environments.

## References

- [1] T. Ando, *J. Phys. Soc. Jpn.* 66, 1066 (1997)
- [2] F. Wang, G. Dukovic, L. E. Brus, and T. F. Heinz, *Science* 308, 838 (2005)
- [3] L. Cognet, D. A. Tsyboulshi, J.-D. R. Rocha, C. D. Doyle, J. M. Tour, and R. B. Weisman, *Science* 316, 1465 (2007)
- [4] L. L'uer, S. Hoseinkhani, D. Polli, J. Crochet, T. Hertel, and G. Lanzani, *Nature Phys.* 5, 54 (2009).
- [5] C. Georgi, M. Böhmler, H. Qian, L. Novotny, and A. Harschuh, *Phys. Status Solidi B* 246, 2683 (2009).
- [6] A. J. Siitonen, D. A. Tsyboulski, S. M. Bachilo, and R. B. Weisman, *Nano Lett.* 10, 1595 (2010).
- [7] S. Moritsubo, T. Shimada, Y. Murakami, S. Chiashi, S. Maruyama, and Y. K. Kato, *Phys. Rev. Lett.* 104, 247402 (2010).
- [8] K. Yoshikawa, K. Matsuda, and Y. Kanemitsu, *J. Phys. Chem. C* 114, 4353 (2010).
- [9] H. Liu, D. Takagi, S. Chiashi, and Y. Homma, *Nanotechnology* 20, 345604 (2009).
- [10] Y. Homma, S. Suzuki, Y. Kobayashi, M. Nagase, and D. Takagi, *Appl. Phys. Lett.* 84, 1750 (2004).
- [11] J. Lefebvre, Y. Homma, and P. Finnie, *Phys. Rev. Lett.* 90, 217401 (2003).
- [12] S. M. Bachilo, M. S. Strano, C. Kittrell, R. H. Hauge, R. E. Smalley, and R. B. Weisman, *Science* 298, 2361 (2002).
- [13] R. B. Weisman and S. M. Bachilo, *Nano Lett.* 3, 1235 (2003).
- [14] S. Chiashi, S. Watanabe, T. Hanashima, and Y. Homma, *Nano Lett.* 8, 3097 (2008).
- [15] Y. Murakami and J. Kono, *Phys. Rev. Lett.* 102, 037401 (2009).
- [16] Y.-F. Xiao, T. Q. Nhan, M. W. B. Wilson, and J. M. Fraser, *Phys. Rev. Lett.* 104, 017401 (2010).
- [17] K. Matsuda, T. Inoue, Y. Murakami, S. Maruyama, and Y. Kanemitsu, *Phys. Rev. B* 77, 033406 (2008).
- [18] T. Hertel, R. E. Walkup, and P. Avouris, *Phys. Rev. B* 58, 13870 (1998).
- [19] L. Yang and J. Han, *Phys. Rev. Lett.* 85, 154 (2000).
- [20] A. Hagen, M. Steiner, M. B. Raschke, C. Lienau, T. Hertel, H. Qian, A. J. Meixner, and A. Hartschuh, *Phys. Rev. Lett.* 95, 197401 (2005).
- [21] Y.-Z. Ma, L. Valkunas, S. L. Dexheimer, S. M. Bachilo, and G. R. Fleming, *Phys. Rev. Lett.* 94, 157402 (2005).
- [22] A. Högele, C. Galland, M. Winger, and A. Imamoglu, *Phys. Rev. Lett.* 100, 217401 (2008).
- [23] Y. Ohno, S. Iwasaki, Y. Murakami, S. Kishimoto, S. Maruyama, and T. Mizutani, *Phys. Status Solidi B* 244, 4002 (2007).
- [24] J. Lefebvre, D. G. Austing, J. Bond, and P. Finnie, *Nano Lett.* 6, 1603 (2006).

- [25] Y. Miyauchi, H. Hirori, K. Matsuda, and Y. Kanemitsu, Phys. Rev. B 80, 081410R (2009)
- [26] A. Srivastava, and J. Kono, Phys. Rev. B 79, 205407 (2009)
- [27] Y. Murakami, and J. Kono, Phys. Rev. B 80, 035432 (2009)
- [28] M. Islam, D. E. Milkic, C. L. Kane, A. G. Yodh, and J. M. Kikkawa, Phys. Rev. Lett. 93, 037404 (2004)
- [29] S. Berciaud, L. Cognet, and B. Lounis, Phys. Rev. Lett. 101, 077402 (2008)
- [30] J. Xie, T. Inaba, R. Sugiyama, and Y. Homma, Phys. Rev. B 85, 085434 (2012)

# Chapter 4

## Atmospheric Ions as an Origin of Photoinduced Degradation

### 4.1 Introduction

Electrical properties of SWCNTs depend on the tube chirality [1]. Excited states of semiconducting SWCNTs can be produced by not only electrical but also optical means [2] because they are direct band gap semiconductors with an emission energy of approximately 1 eV. The emission energy of SWCNTs is close to the telecom wavelength and can be tuned by atmosphere [3]-[5] and external fields [6]. Furthermore, SWCNTs have unique one-dimensional structure and high charge carrier mobility up to 10,000 cm/V·s [7]. These properties make SWCNTs one of the best materials for optoelectronic devices such as a nanoscale light source [2]. Emission instability at a high excitation regime is one of the problems to be solved for the application of SWCNTs to such devices [8]-[11]. In PL experiments of SWCNTs, the deviation from linear fitting at low excitation regime on the emission versus excitation intensity plot for PL from an SWCNT, i.e. EEA, is firstly observed. Further increasing excitation power then causes saturation and temporal fluctuation of PL emission intensity [8]-[10]. Finally, decrease in time averaged intensity, in many cases, along with decreasing emission energy of PL from the SWCNT [10][11] are observed for the high excitation regime. The reduction of PL intensity is irreversible and thought to be due to some chemical reaction caused by the excitation of SWCNT. A similar phenomenon is observed in the electroluminescence experiment of an SWCNT [12]. While the decrease of emission intensity in many photo- and electroluminescence experiments was attributed to the effect of electrostatic doping, the origin of the change in emission energy was not clear. Deep understanding of these photoinduced phenomena is needed for the application of SWCNTs to optoelectronic devices.

In this chapter, we demonstrate that the exposure of an air-suspended SWCNT to atmospheric ions generated by corona discharge degrades the intensity and causes a low energy shift of PL peak position. These changes were accelerated by laser illumination. Atmospheric ions are present, though sparse, all the time. Thus, the reaction between SWCNTs and atmospheric ions can potentially occur everywhere; even an "as-grown" sample is possibly affected by the reaction. Note that, the generation of atmospheric ions using corona discharge has often been employed for atmospheric science for simulating naturally generated atmospheric ions in air [13][14].

### 4.3 Experiment

Air-suspended SWCNTs used for this experiment were directly grown by CVD on a fused silica substrate with optically patterned micro-pillars [15]. The pair of micro-pillars was positioned 10  $\mu\text{m}$

apart and the height of the pillars was 8  $\mu\text{m}$ . For the CVD, cobalt nanoparticle were used as the catalyst, and ethanol as the source gas. After the growth, PL spectroscopy was performed for individual SWCNTs under laboratory atmosphere. The detail of CVD condition is explained in chapter 2. The Ti:sapphire laser was used for excitation. Excitation energy was tuned from 1.50 to 1.75 eV. The laser power was adjusted to 100  $\mu\text{W}$  and the laser spot to 1-2  $\mu\text{m}$  in diameter, which corresponded to a laser power density of 3  $\text{kW}/\text{cm}^2$ . Generally, a laser power density below 50  $\text{kW}/\text{cm}^2$  does not cause photoinduced degradation such as bleaching or blinking of PL from SWCNTs [11]. PL ranging from 0.85 to 1.25 eV in energy was collected with an InGaAs multiarray detector. After assigning the chirality of an SWCNT from a PLE map, the substrate was placed about 15 cm away from the air ionizer (BF-SZAI, Shishido Electrostatic Ltd., Japan). The air ionizer had point-to-plate configuration electrodes where atmospheric ions were generated by corona discharge. Atmospheric ions were sent to the substrate by blowing air from a fan. No acceleration voltages was applied for this experiment. The density of generated cation was  $5.1 \times 10^{10}/\text{m}^3$ , while that of anion was  $3.6 \times 10^{10}/\text{m}^3$ . Atmospheric ions increased to the order of  $10^{10}/\text{m}^3$  from a typical density of  $10^3/\text{m}^3$  in the natural environment [13] by using the air ionizer. After the exposure of the SWCNT to atmospheric ions, PL measurements were again conducted.

#### 4.5 Degradation due to Exposure to High Atmospheric Ion Flux

Figure 4.1a shows the PLE map of the SWCNT grown between the pair of pillars before exposure to atmospheric ions. The chirality of the SWCNT was assigned to (11,3) from the PLE map [16]. Figure 4.1b shows the emission spectra from the SWCNT before and after exposure to atmospheric ions. The SWCNT was exposed to atmospheric ions for an hour with keeping the excitation laser off. A low energy shift of emission energy by 4.9 meV as well as a decrease of the integrated intensity from its original value by a factor of over 2 were observed after exposure. Lorentzian fittings (indicated by

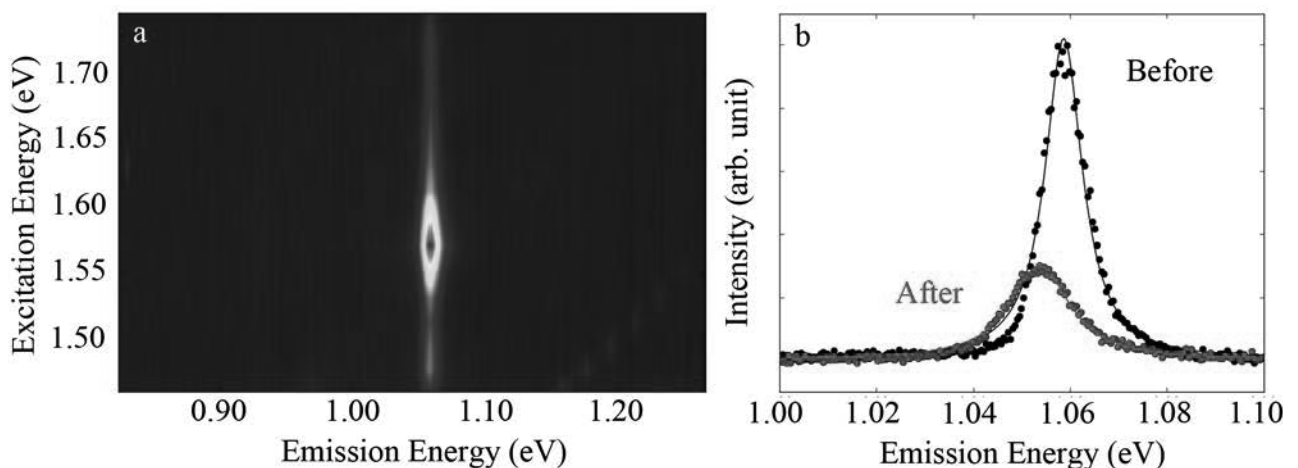


Fig. 4.1. (a) PL excitation map of the (11,3) nanotube suspended between two micropillars. (b) Emission spectra of the (11,3) nanotube shown in (a) before and after exposure to atmospheric ions. Solid lines are Lorentzian fittings of corresponding data plots. Reprinted with permission from [41].

solid lines in Fig. 4.1b) of the spectra revealed an increase of FWHM by 5.4 meV. In addition to emission, absorption peak energy sifted slightly to lower energy by 3.0 meV.

Raman spectra of the (9,8) nanotube before and after the exposure to high atmospheric ion flux are shown in Fig. 4.2. Arrows in Fig. 4.2a indicate maximum intensities of G-mode at 1590  $\text{cm}^{-1}$  for each spectrum. G-mode Raman feature is caused by the stretching of the C-C bond in graphitic materials [17]. G-mode intensity after exposure was reduced to 80% of its original value, which means photon absorption is still maintained after exposure to high atmospheric ion flux. On the other hand, corresponding PL spectra are shown in the inset of Fig. 4.2a and the reduction of PL intensity close to 20% of its original value was observed after exposure to high atmospheric ions. The reduction of PL intensity is larger than that of Raman intensity. Therefore, bleaching of absorption is unlikely to be the cause of the reduction in PL intensity.

The D-mode at 1300-1350  $\text{cm}^{-1}$  characterizes disorder in  $\text{sp}^2$  hybridized carbon system [17]. The ratio of G-mode intensity to D-mode intensity, which is referred to as G/D ratio, represents the quality of graphitic materials. The higher the G/D ratio, the higher the quality of graphitic materials. Raman spectra after the exposure confirmed that the intensity of D-mode at 1300  $\text{cm}^{-1}$  slightly increased (see Fig. 4.2b) resulting in the decrease of G/D ratio to 10. Before exposure, on the other hand, the D-band intensity from the SWCNT was below the noise level of the Raman measurement. Usually, G/D ratio over 100 is expected for higher fluorescent SWCNTs as shown in Fig. 4.2. The G/D ratio was large compared to the result of  $\text{Ga}^+$  irradiation [18] which showed G/D ratio below 1 after the irradiation. Even though the G/D ratio below 1 was observed, tubular structure of SWCNTs

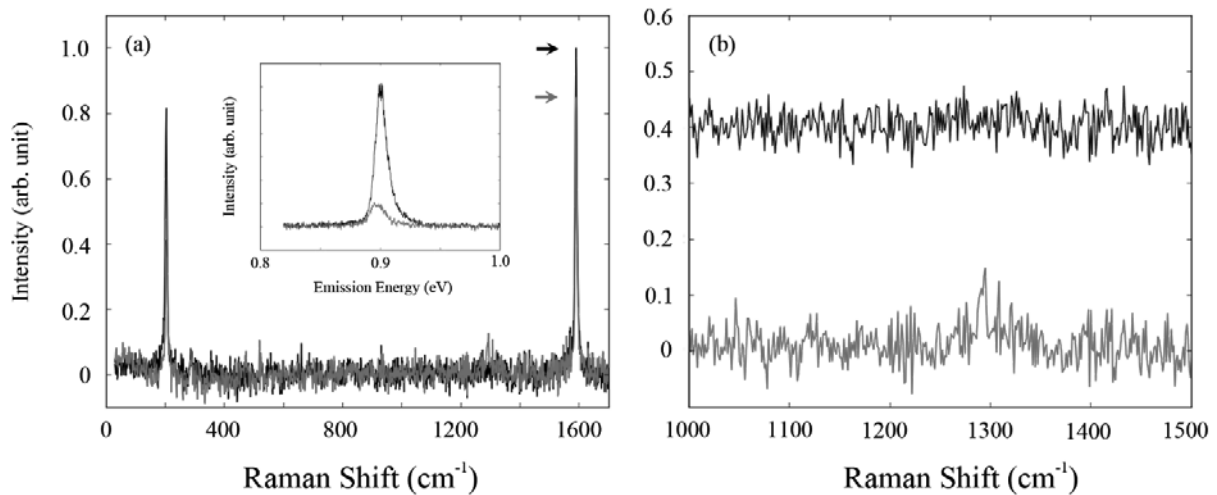


Fig. 4.2 (a) Raman spectra before (black) and after (red) the exposure to high atmospheric ion flux. The inset is corresponding PL spectra. (b) Expanded plot of the range from 1000-1500  $\text{cm}^{-1}$  in (a). Raman spectrum before exposure is shifted upward by 0.4 for the easiness of comparison.

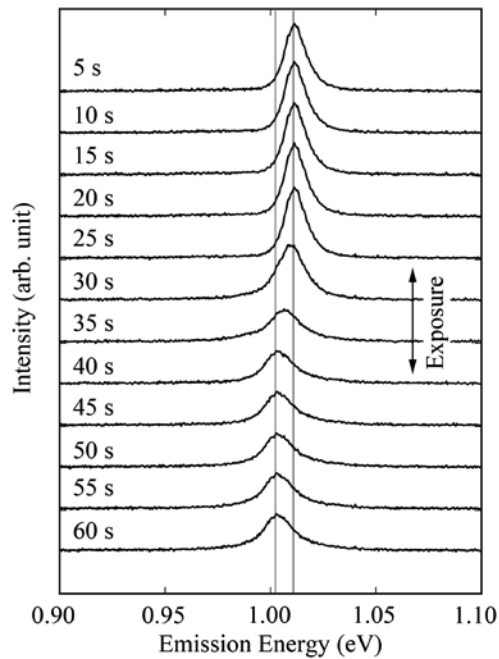


Fig. 4.3. Sequential emission spectra of the (10,5) nanotube suspended between micropillars for 60 seconds. Atmospheric ions were blown onto the SWCNT at 25-35 seconds. Reprinted with permission from [41]

was still maintained [18]. Hence, the reaction was not destructive enough to collapse the tubular structure of SWCNTs. Note that the ratio of RBM intensity to G-mode intensity also decreased to half. The decrease of RBM intensity suggests that the crystal ordering of the SWCNT along the circumference direction became lowered by exposure to high atmospheric ion flux.

#### 4.4 Acceleration of the Reaction by the Excitation of SWCNTs

Next, we show that the reaction was strongly accelerated by laser illumination. Figure 4.3 shows sequential emission spectra from the (10,5) nanotube measured for 60 seconds. Excitation energy was set to 1.59 eV, corresponding to  $E_{22}$  excitation of the (10,5) nanotube. In addition to laser illumination for the entire time, atmospheric ions were blown on the SWCNT at 25-35 seconds. Change in PL intensity as well as a low energy shift of the peak position were observed only during the blowing of atmospheric ions. Again, laser power density used for each experiment was below  $3 \text{ kW/cm}^2$ , and photoinduced bleaching is usually not observed at that power [10][11]. In fact, bleaching was not observed until the blowing of atmospheric ions started. On the other hand, exposure of an SWCNT to high ion flux itself did not cause significant change in PL; it took over an hour for the spectrum to change without laser illumination as shown in Fig. 4.1. It is clear that laser illumination accelerated the reaction between an SWCNT and atmospheric ions.

Figure 4.4 shows excitation energy dependence of the reaction between atmospheric ions and the (9,8) nanotubes. Excitation energy dependence of PL from the SWCNT was firstly measured in order to confirm  $E_{22}$  energy of the SWCNT as shown in Fig. 4.4a. Maximum absorption

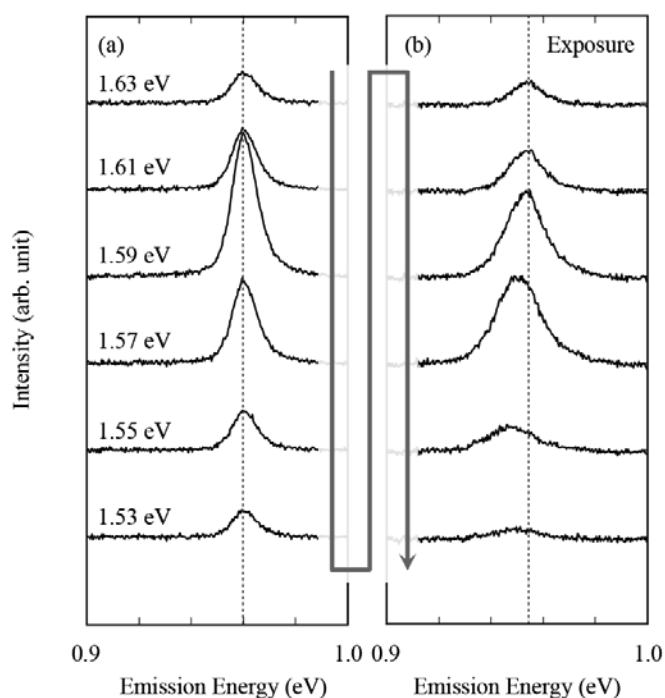


Fig. 4.4 (a) Excitation energy dependence of the reaction between atmospheric ions and the (9,8) nanotube. (b) The result of similar measurement as (a) with exposing the SWCNT to high atmospheric ion flux.

corresponding to  $E_{22}$  energy of the (9,8) nanotube was observed at excitation energy of 1.59 eV. No spectral shift was observed because the SWCNT was not exposed to high atmospheric ion flux in Fig. 4.4a. Then, similar measurement was carried out with exposing the SWCNT to high atmospheric ion flux. As shown in Fig. 4.4b, low energy shift of PL peak position was observed after the excitation energy passed the maximum absorption of the (9,8) nanotubes. Note that difference in initial peak position between Fig. 4.4a and 4.4b is due to the fact that the same measurements as Fig. 4.4b were carried out in advance. Initial peak position gradually shifts lower for every experiment because photoinduced bleaching as shown in Fig. 4.4b is irreversible. The reaction was sensitive to the excitation of SWCNTs. Therefore, the possibility that the optical excitation of environmental media such as water, oxygen, or atmospheric ions accelerates the reaction is eliminated. From the experimental results above, we conclude that the atmospheric ions is the origin of photoinduced degradation of PL from SWCNTs.

#### 4.5 Reduction of Photoluminescence Intensity due to Exciton Localization

It was shown that the doping of free charges to an SWCNT causes both reduction of PL intensity and a low energy shift of PL peak position via the screening of Coulomb interaction exerting on an exciton

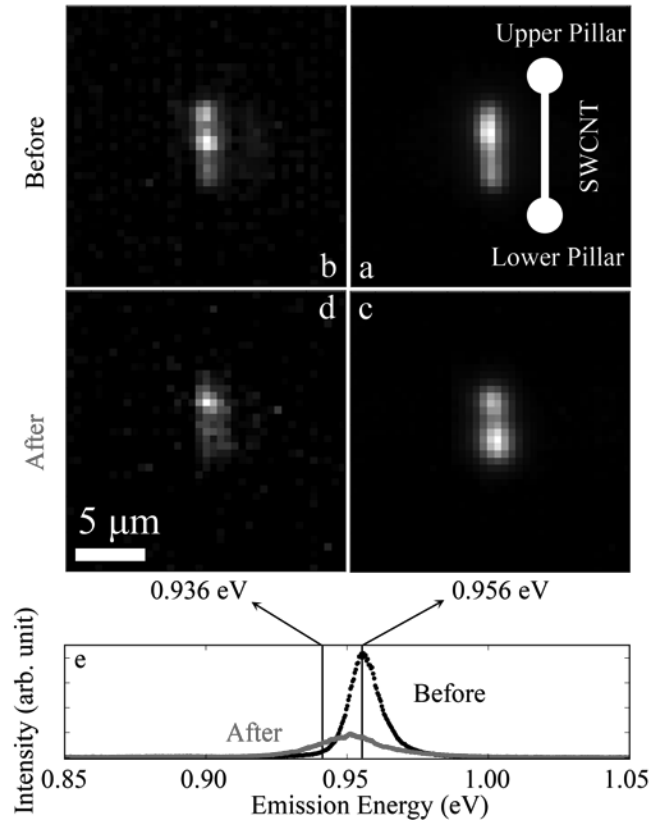


Fig. 4.5. PL imaging of (9,7) nanotube suspended between two micropillars (a, b) before and (c, d) after exposure to atmospheric ions. (e) Corresponding emission spectra before and after exposure to high ion flux. Reprinted with permission from [41].

[12]. However, this logic cannot be applied to our results because the effect of laser illumination was a local phenomenon. Figure 4.5 shows PL imaging of a (9,7) nanotube before (a, b) and after (c, d) exposure to atmospheric ions. The suspended SWCNT was set longitudinally in the image as shown in Fig. 4.5a. Two images on the right (a, c) are PL imagings at the emission energy of 0.956 eV, corresponding to the peak energy of the original emission spectrum. On the other hand, images on the left (b, d) are that of 0.936 eV at which the intensity after exposure surpasses that of before. Hence, PL imagings of Fig. 4.5b and 4.5d accent the emission feature due to the reaction. Photoluminescence intensity of the SWCNT before the exposure was slightly off centered to the upper side in both Fig. 4.5a and 4.5b. This means, although the intensity is inhomogeneous, the emission peak energy was almost the same along the entire length of the SWCNT before the exposure. During exposure to high ion flux, the laser spot irradiated a point 3  $\mu\text{m}$  apart from the upper edge of the suspended SWCNT. After the exposure, PL at the emission energy of 0.936 eV was centered at the point on which the laser was focused as shown in Fig. 4.5d. On the other hand, as shown in Fig. 4.5c, the emission of 0.956 eV from the same region was dimmer than that from the lower half. This means the reaction occurred selectively at the region illuminated by the laser light.

One possible reason for the decrease of PL intensity is the creation of exciton localization site due to the partial  $sp^3$  hybridization of carbon atoms in the SWCNT. Multi phonon decay provides

effective non-radiative decay path with the decay time of 100 ps range for localized excitons. The local reduction of PL intensity as shown in Fig. 4.5d supports the MPD as one of the major mechanisms of the reduction in PL intensity rather than the effect of mobile charges. The introduction of a single exciton localization site can bleach PL over a 100-200 nm long section of the SWCNT, corresponding to the intrinsic exciton diffusion length [19], and modify exciton distribution in the SWCNT [20][21]. For surfactant wrapped SWCNTs, the local reduction of PL on the order of 10 nm was observed by tip-enhanced near-field optical microscopy [22].

#### **4.6 Low Energy Shift of Photoluminescence Peak Position due to the Attachment of Water Cluster Ions**

We assume that the low energy shift of PL peak position is due to the change in dielectric environment around an SWCNT [3]-[5]. The diameter of an SWCNT is typically ranging 1-3 nm, and the electric field line of an exciton protrudes out of the surface. Because of this, exciton binding energy is sensitive to the change of dielectric environment around the nanotube surface. Water molecule can be the candidate for the dielectric medium that involve the change in dielectric environment around SWCNTs. Water has a relatively large dielectric constant among components of air. Furthermore, atmospheric ions are often found to be in water cluster ions  $Y(H_2O)_n$ , where Y is the core ion and n is an integer [23]. In other words, a core ion attached to the SWCNT surface supplies hydrophilicity to the SWCNT. Recent research revealed that an as-grown SWCNT suspended in air is covered with thin water layers [5]. The attachment of water layers causes a low energy shift of PL peak position by 25 meV from the emission peak position of the SWCNT in vacuum. In our results, additional water molecules along with the core ion itself possibly attach to the nanotube surface. We assume the hydronium ion “ $H_3O^{+}$ ” as the core ion of the water cluster ion. That is because, first, reaction between ionic species and nonpolar  $sp^2$  carbon network exclusively occurs for cations because nucleophilic attack is restricted for nonpolar  $sp^2$  carbon network. On the other hand, electrophilic reactions are likely to occur as seen in electrophilic aromatic substitution, Friedel-Crafts reaction and so on. This can also be understood by the fact that holes are originally doped to SWCNTs used for the channels of field effects transistors [2]. Second, past researches in the field of atmospheric science revealed the dominant generation of hydronium ions with positive corona discharge [24]-[26]. Hydronium ion is dominantly generated by corona discharge in many vapor conditions as long as they contain water molecules at least 0.04 mol % [27]. Third, we observed larger amount of cation than anion as a results of atmospheric ion generation by corona discharge. For those reasons, we assume a hydronium ion along with water molecules to be a major chemical species relating to the reaction.

#### **4.7 Hydronium Ion as Proton Donor**

Hydronium ion can be the source of proton to the nanotube surface, which reproduces the environment in acidic solution. Simulation based on density functional theory carried out for explaining the chemical reaction in acidic solution predicted that two local minimum of chemical structure exist

when proton and singlet oxygen approach the nanotube surface [30]. One is hydroperoxide, and the other is hydroxide along with epoxide. On the other hand, the effect of oxygen to photoinduced degradation of SWCNTs in air has been well discussed so far. It is fair to attribute degradation in air to oxygen. However, critical mechanisms for the reaction is not established yet. This may be due to overlooking of the presence of proton donor in air. Here, the importance of hydronium ion for the photoinduced degradation in air allows us to reason that similar mechanisms as seen in acidic solution can be applied to photoinduced degradation in air. It should be noted that corona discharge we used for increasing atmospheric ions also generates ozone as well as excited oxygen as the predecessor [14][28]. Those oxygen species itself are thought to be the cause of photoinduced degradation [29][30]. Here, those oxygen species may also provide singlet oxygen to the nanotube surface. If both proton and singlet oxygen generated by corona discharge come together on the nanotube surface, the degradation as seen in acid solution will occur just with exposure. Actually, the reaction occurred only with exposure to high atmospheric ion flux as shown in Fig. 4.1. However, the density of those excited oxygen species was below 0.04 ppm, and we assume this value is quite low. Therefore, we conclude that the excited oxygen species generated by corona discharge did not leave significant effect on our results. This is consistent with the reaction time longer than an hour for the reaction as shown in Fig. 4.1.

#### 4.8 Effect of Laser Illumination

Next, we discuss the effect of laser illumination on the reaction. The reaction assisted by laser illumination resulting in monotonic decrease of PL intensity is often referred to as photoinduced bleaching. Photoinduced bleaching of SWCNTs was found in the early stages of research on PL from SWCNTs [31][32]. We focus on photoexcited exciton in an SWCNT for describing the reaction. As shown in Fig. 4.5, this reaction accelerated exclusively at the point a laser spot irradiates. Furthermore,

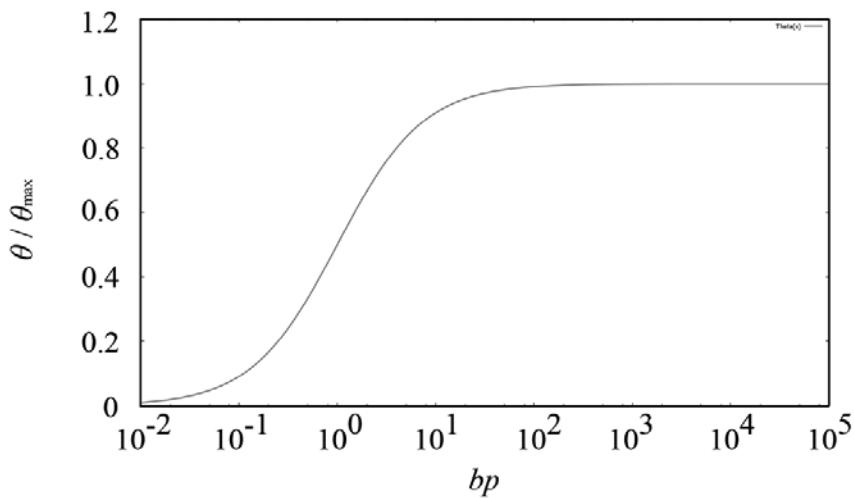


Fig. 4.6 Line plot of  $\theta/\theta_{\max}$  as a function of  $bp$ .

considering the acceleration of the reaction by laser illumination with photon energy corresponding to  $E_{22}$  absorption of the SWCNT, it is clear that the increase of excited exciton accelerated the reaction between hydronium ions and SWCNTs. Because the exciton diffusion length is on the order of  $10^2$  nm [33], the reaction area is almost equal to the laser illumination point. On the other hand, due to high thermal conductivity of SWCNTs up to  $3 \times 10^3$  W/m·K [34][35], the possibility that the reaction was accelerated by a temperature increase is excluded.

The laser illumination possibly triggers the generation of chemical bonds between hydronium ions, oxygen, and the SWCNT. If so, we can divide the entire reaction process into two steps. First step is physisorption of hydronium ions and oxygen as the source of proton and ground state oxygen on the nanotube surface. At this step, the coverage  $\theta$  for the absorption of each gas species on the SWCNT would follow Langmuir equation;

$$\theta = \theta_{\max} \frac{bp}{(1+bp)} \quad (4.1)$$

where  $\theta_{\max}$  is the saturating coverage,  $b$  the equilibrium constant, and  $p$  the partial pressure of hydronium ion or oxygen in air. The coverage dramatically increases in the range  $10^{-1}$ - $10^1$  as shown in Fig. 4.6. On the other hand, small change in the coverage can be seen for  $bp$  over  $10^1$ . The coverage does not increase linearly as the partial pressure in Langmuir absorption. Therefore, the large generation rate of atmospheric ions by corona discharge in our experiment does not provide information on the reaction rate. The reaction rate is determined by the saturating coverage at the high partial pressure range. The saturating coverage  $\theta_{\max}$  would be small. For example, the saturating coverage between 0.2-0.3 was reported for Ar and Kr absorption [36]. Furthermore, we now assume simultaneous absorption of hydronium ions and oxygen. Hence,  $\theta_{\max}$  would be further reduced from values for the independent absorption of hydronium ions and oxygen. Because of the low coverage of physisorption, the change in an emission spectrum would not occur at this time. Second step is the excitation of absorbed oxygens to singlet oxygens.

The excitation of absorbed oxygen is probably due to the relaxation of excitons in SWCNTs via Förster resonance energy transfer between the SWCNT and absorbed oxygen. Förster resonance energy transfer for two bundled SWCNTs were already reported [37]. The excitation of a singlet oxygen energetically lying 1.07 eV above the ground state can be achieved by the relaxation of an  $E_{11}$  singlet exciton [38]. Once a singlet oxygen is generated, hydroxyl group and epoxide on the nanotube surface are created, and then desorption rate of those functional groups significantly decreases, which means the increasing coverage of functional groups on the nanotube surface. As seen in Fig. 4.3, it took 10 seconds to cause the change in the spectrum. Thus, the reaction rate for the generation of chemical bond was not very high at this excitation intensity. The amount of ion flux was not the major factor determining the reaction rate because of the limited saturating coverage of physisorption.

## 4.9 Discussion on Photoinduced Blinking

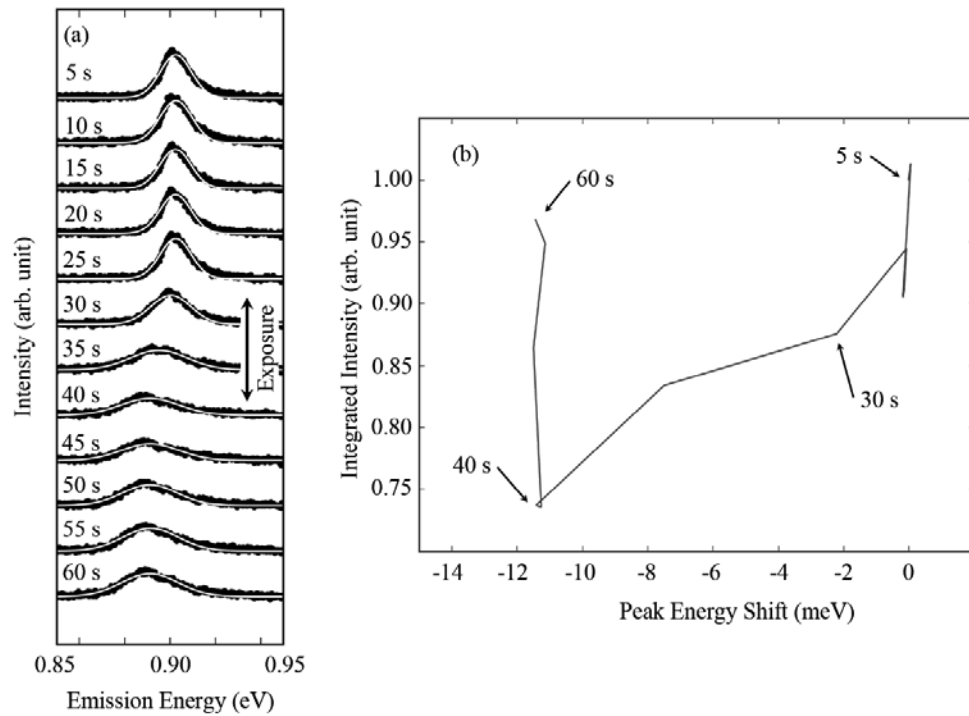


Fig. 4.7 (a) Sequential emission spectra of the (9,8) nanotube suspended between micropillars for 60 seconds. Atmospheric ions were blown onto the SWCNT at 25-35 seconds. (b) Corresponding Peak energy shift versus integrated intensity change plot for the spectra shown in (a). Integrated intensities are normalized at the initial integrated intensity, and peak energy shift is the difference from initial emission peak energy.

Next, we discuss blinking observed when SWCNTs were exposed to high atmospheric ion flux. Figure 4.7a shows the sequential emission spectra of the (9,8) nanotube, which was obtained by the same measurement as Fig. 4.3, while Fig. 4.7b is the corresponding peak energy shift versus integrated intensity change plot for the spectra shown in (a). Each integrated intensity and emission peak position was obtained by Gaussian fitting of the corresponding emission spectrum (white solid line in Fig. 4.7a). As shown in Fig. 4.7b, the decrease of integrated intensity and emission peak position started at 25-30 second corresponding to the duration of exposure to high atmospheric ion flux. Integrated intensity was decreased to 75% of its original value at 40 s. After the end of exposure, the recovery of integrated intensity occurred while emission peak position was kept lowered. Non-monotonic change in the integrated intensity implies that atmospheric ions can be not only the origin of bleaching but also the origin of blinking of PL from SWCNTs. However, only the small number of SWCNTs showed the recovery of integrated intensity among nanotube samples employed for experiments in this thesis. This may be due to the large concentration of atmospheric ions generated by corona discharge.

Integrated intensity recovered to almost its original value in Fig. 4.7b, which supports the mechanisms for photoinduced blinking where the fluctuation of PL intensity occur due to the

absorption and desorption of chemical species on the nanotube surface. On the other hand, possibility that blinking occurs due to the mobile charged diffusing in SWCNTs with the energy barrier is less likely. This is because the nanotube segment where the mobile charges is located and decreased PL intensity observed is inevitably present in the description attributing blinking to diffusing mobile charges. Therefore, full recovery of PL intensity as shown in Fig. 4.7b is not explained by diffusing mobile charges.

The non-linear relation on peak energy shift versus integrated intensity change plot also supports the difference between the mechanisms for the decrease of PL intensity and low energy shift of peak position, which is discussed above.

#### 4.10 Recovery from Degraded Photoluminescence

If the assignment of chemical species contributing photoinduced degradation is possible, the recovery methodology from degraded PL will be proposed. Here, we presumed the creation of hydroxyl group on the nanotube surface was the major products of photoinduced degradation. The situation in which hydroxyl group attaches to a graphitic surface is analogous to graphene oxide (GO). Therefore, recovery from degraded PL of SWCNTs is possibly achieved in the same manner as GO is reduced. Graphene oxide was reduced by high temperature annealing resulting in graphene with the higher intensity ratio of 2D-mode to G-mode in Raman spectra [39]; the intensity ratio of 2D-mode to G-mode in graphene Raman spectra represents the degree of abundance for  $sp^2$  bonding in graphitic structure.

Although repeatability was not examined at this time, high temperature annealing of an SWCNT which suffer the photoinduced degradation was conducted for reference. Figure 4.8 shows PL spectra of a (9,8) nanotube. In Figure 4.8, photoluminescence spectra of the original SWCNT, after exposed to high atmospheric ions, and after annealed in Ar/H<sub>2</sub>(3%) mixed gas atmosphere are shown in black, red, and blue, respectively. All of the spectra were obtained in air. The annealing in Ar/H<sub>2</sub> atmosphere was conducted for an hour with the temperature of 950 °C. After exposure to high atmospheric ion flux, PL intensity decreased and emission energy shifted lower as discussed above. The shift amount of peak position was 3 meV, and integrated PL intensity decreased 40% of its original value. On the other hand, successive annealing in Ar/H<sub>2</sub> gave rise to the high energy shift of the emission peak position by 28 meV. In addition to high energy shift of emission peak energy, further decrease in integrated PL intensity was observed after the annealing. However, the decrease in PL intensity was moderate, and we assume that the serious damage were not induced to the SWCNT by high temperature annealing and that the small decrease in PL intensity was due to the hydrogen attack to the nanotube surface. In fact, small satellite peak approximately 120 meV below the main peak was observed, indicating attachment of hydrogen atom onto the nanotube surface [34].

High energy shift of PL intensity is expected when absorbed water on the nanotube surface is removed. Therefore, annealing in Ar/H<sub>2</sub> may remove surface hydroxyl group with hydrated water. Interestingly, the peak position after annealing was higher than that of the as-grown SWCNT,

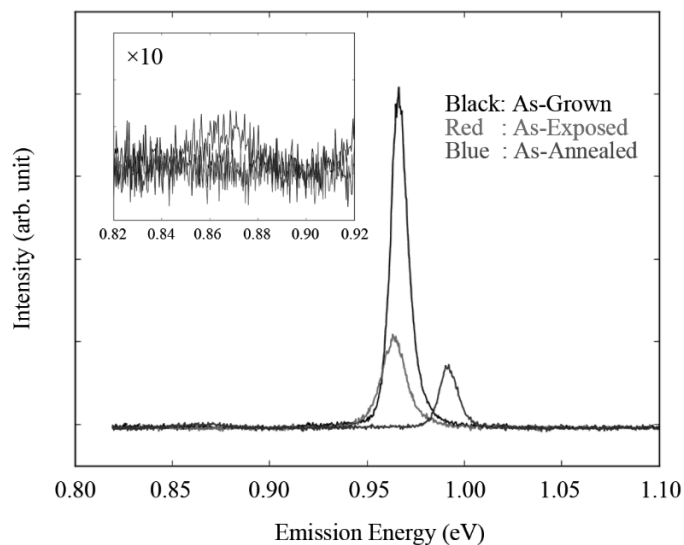


Fig. 4.8 Sequential PL spectra of an SWCNT. Photoluminescence spectra of As-grown SWCNT, SWCNT after exposed to high atmospheric ion flux, and after Ar/H<sub>2</sub> anneal are shown in black, red, and blue, respectively.

implying that SWCNTs was originally affected by the attachment of some functional groups. While the functional groups which increased hydrophilicity on the nanotube surface seems to have been removed by high temperature annealing, integrated PL intensity was still low compared to its original value. Therefore, the decrease in PL intensity and low energy shift of peak position due to the attachment of atmospheric ions were likely to be caused by different mechanisms. This supports the discussion above where the decrease in PL intensity was due to the creation of exciton localization site followed by MPD at the position while low energy shift was attributed to the change in dielectric environment caused by the attached hydrated hydronium ions.

High temperature annealing in Ar/H<sub>2</sub> atmosphere was not enough to recover the PL intensity. Although the serious damage was not induced by high temperature annealing, the attachment of hydrogen onto the nanotube surface occurs. On the other hand, hydrophilicity of the nanotube surface was considerably reduced. The generation of C-H bonding at the position where hydroxyl group attached to carbon might occur due to the high temperature annealing in Ar/H<sub>2</sub> atmosphere. Therefore, introduction of carbon source instead of hydrogen possibly recovers the PL intensity. In fact, introduction of ethanol vapor in hydrogen gas further increased 2D/G ratio of graphene Raman spectra [39]. Further study is needed for the verification in this regard.

#### 4.11 Summary

The weakening and low energy shift of PL from suspended SWCNTs were observed when SWCNTs were exposed to high atmospheric ion flux. The reaction was accelerated by laser illumination. These results were attributed to chemisorption of atmospheric ions together with water

molecules. We assume hydronium ions to be the core ions. We emphasize that atmospheric ions are possible candidates for the cause of photoinduced bleaching and blinking of SWCNTs in air because atmospheric ions exist, though sparse, all the time in air. Furthermore, the reaction has the potential of high-spatial-resolution chemical doping to SWCNTs by combining the technique of this reaction with near-field optics, and changing cationic species.

## References

- [1] S. Iijima, and T. Ichihashi, *Nature* 363, 603 (1993)
- [2] P. Avouris, M. Freitag, and V. Perebeinos, *Nat. Phot.* 2, 341 (2008)
- [3] S. Chiashi, S. Watanabe, T. Hanashima, and Y. Homma, *Nano Lett.* 8, 3097 (2008)
- [4] Y. Ohno, S. Iwasaki, Y. Murakami, S. Kishimoto, S. Maruyama, and T. Mizutani, *Phys. Rev. B* 73, 2354.37 (2006)
- [5] Y. Homma, S. Chiashi, T. Yamamoto, K. Kono, D. Matsumoto, J. Shitaba, and S. Sato, *Phys. Rev. Lett.* 110, 157402 (2013)
- [6] M. Freitag, M. Steiner, A. Naumov, J. P. Small, A. A. Bol, V. Perebeinos, and P. Avouris, *Am. Chem. Soc. Nano* 3, 374.5 (2009)
- [7] X. Zhou, J.-Y. Park, S. Huang, J. Liu, and P. L. McEuen, *Phys. Rev. Lett.* 95, 146805 (2005)
- [8] J. J. Crochet, J. G. Duque, J. H. Werner, and S. K. Doorn, *Nat. Nanotech.* 7, 126 (2012)
- [9] L. Cognet, D. A. Tsyboulski, J.-D. R. Rocha, C. D. Doyle, J. M. Tour, R. B. Weisman, *Science* 316, 1465 (2007)
- [10] P. Finnie and J. Lefebvre, *Am. Chem. Soc.* 6, 1702 (2012)
- [11] C. Georgi, N. Hartmann, T. Gokus, A. A. Green, M. C. Hersam, and A. Hartschuh, *Chem. Phys. Chem.* 9, 1460 (2008)
- [12] M. Steiner, M. Freitag, V. Perebeinos, A. Naumov, J. P. Small, A. A. Bol, and P. Avouris, *Nano Lett.* 9, 3477 (2009)
- [13] A. Hirsikko, T. Nieminen, S. Gagné, H. E. Manninen, M. Ehn, U. Hörrak, V.-M. Kerminen, L. Laakso, P. H. McMurry, A. Mirme, S. Mirme, T. Petäjä, H. Tammet, V. Vakkari, M. Vana, and M. Kulmala, *Atmos. Chem. Phys.* 11, 767 (2011)
- [14] J. S. Chang, P. A. Lawiess, and T. Yamamoto, *Trans. Plas. Sci.* 19, 1152 (1991)
- [15] J. Lefebvre, Y. Homma, and P. Finnie, *Phys. Rev. Lett.* 90, 217401 (2003)
- [16] J. Lefebvre and P. Finnie, *Phys. Rev. Lett.* 98, 167406 (2007)
- [17] M. S. Dresselhaus, A. Jorio, M. Hofmann, G. Dressehaus, and R. Saito, *Nano Lett.* 10, 751 (2010)
- [18] Y. J. Jung, Y. Homma, R. Vajtai, Y. Kobayashi, T. Ogino, and P. M. Ajayan, *Nano Lett.* 4, 1109 (2004)
- [19] A. J. Siitonen, D. A. Tsyboulski, S. M. Bachilo, and R. Bruce Wiseman, *Phys. Chem. Lett.* 1, 2189 (2010)
- [20] D. M. Harrah, and A. K. Swan, *Am. Chem. Soc. Nano* 5, 647 (2011)
- [21] T. Hertel, S. Himmelein, T. Ackermann, D. Stich, and J. Crochet, *Am. Chem. Soc. Nano* 12, 7161

(2010)

- [22] C. Georgi, A. A. Green, M. C. Hersam, and A. Hertscuh, *ACS Nano*, 4, 5914 (2010)
- [23] K. Sekimoto, and Y. Takayama, *Int. J. Mass Spectrom.* 261, 38 (2007)
- [24] R. S. Narsici, A. D. Bailey, *J. Geophys. Res.* 70, 3687 (1965)
- [25] P. Spanel and D. Smith, *J. Phys. Chem.* 99, 15551 (1995)
- [26] M. Pavlik, and J. D. Skalny, *Rapid Commun. Mass Spectrom.* 11, 1757 (1997)
- [27] M. M. Shahin, *J. Chem. Phys.* 45, 2600 (1966)
- [28] J. Chen and J. H. Davidson, *Plas. Chem. Plas. Proc.* 22, 495 (2002)
- [29] M. S. Strano, C. B. Huffman, V. C. Moore, M. J. O'Connell, E. H. Haroz, J. Hubbard, M. Miller, K. Rialon, C. Kittrell, S. Rameah, R. H. Hauge, and R. E. Smalley, *Reversible*, *J. Phys. Chem. B* 107, 6979 (2003)
- [30] G. Dukovic, B. E. White, Z. Zhou, F. Wang, S. Jockusch, M. L. Steigerwald, T. F. Heinz, R. A. Friesner, N. J. Turro, and L. E. Brus, *J. Am. Chem. Soc.* 126, 15269 (2004)
- [31] T. Savage, S. Bhattacharya, B. Sadanadan, J. Gaillard, T. M. Tritt, Y.-P. Sun, Y. Wu, S. Nayak, R. Car, N. Marzari, P. M. Ajayan, and A. M. Rao, *J. Phys. Cond. Matt.* 15, 5915 (2003)
- [32] M. Zhang, M. Yudasaka, Y. Miyauchi, S. Maruyama, and S. Iijima, *J. Phys. Chem. B* 110, 8935 (2006)
- [33] J. Xie, T. Inaba, R. Sugiyama, and Y. Homma, *Phys. Rev. B* 85, 0854.54 (2012)
- [34] A. M. Marconnet, M. A. Panzer, and K. E. Goodson, *Rev. Mod. Phys.* 85, 1295 (2013)
- [35] E. Pop, D. Mann, Q. Wang, K. Goodson, and H. Dai, *Nano Lett.* 6, 96 (2006)
- [36] Z. Wang, J. Wei, P. Morse, J. Gregory, D. Oscar, E. Vilches, and D. H. Cobden, *Science* 327, 552 (2010)
- [37] J. Lefebvre, and P. Finnie, *J. Phys. Chem. C* 113, 7536 (2009)
- [38] J.-M. Abury, C. Pierlot, J. Rigaudy, and R. Shumidt, *Acc. Chem. Res.* 36, 668 (2003)
- [39] C.-Y. Su, Y. Xu, W. Zhang, J. Zhao, A. Liu, X. Tang, C.-H. Tsai, Y. Huang, and L.-J. Li, *ACS Nano* 9, 5285 (2010)
- [40] K. Nagatsu, S. Chiashi, S. Konabe, and Y. Homma, *Phys. Rev. Lett.* 105, 157403 (2010)
- [41] T. Inaba, and Y. Homma, *Appl. Phys. Lett.* 107, 071907 (2015)

# Chapter 5

## Conclusion and Outlook

Non-linear effects of PL from SWCNTs were mainly discussed in this thesis. There are three regimes in non-linear effects; EEA, photoinduced blinking, and bleaching. Good understanding of those effects is important for the application of SWCNTs to optoelectronic devices especially when the improvement of emission intensity is needed. The improvement of emission intensity increases feasibility of nanotube-based optoelectronic devices. When the optoelectronic application of SWCNTs is realized, communication devices will be further miniaturized, lower energy consumed, and faster operated.

In chapter 3, intrinsic diffusion length and the onset power for EEA was derived from the length dependence of PL intensity using a single SWCNT. Excitons are diffusive in nature in SWCNTs, and exciton mobility is one of the fundamental properties for understanding the optical responses of SWCNTs. Exciton diffusion length depends on the dielectric environment around SWCNTs, and is correlating to PL intensity. Up to now, many experimental studies have been carried out to investigate the exciton diffusion length in semiconducting SWCNTs but leaving large scattering values. Most of those measurements were performed on surfactant- or DNA-wrapped SWCNTs, representing averaged results and preventing a detailed spectral analysis. On the other hand, the use of a single suspended SWCNTs had great advantages for revealing the intrinsic nature of SWCNTs. As the results of the experiment, diffusion length of excitons as long as 200 nm was obtained, which is twice as long as published results. The onset power for EEA was experimentally estimated to  $10^{21}$  photons/cm<sup>2</sup>·s by analyzing the excitation power dependence of PL emission intensity for fixed suspended length as well as the excitation power dependence of exciton diffusion length. Monte Carlo simulation based on experimentally obtained intrinsic diffusion length confirmed the onset power for EEA.

In chapter 4, the origin of photoinduced degradation was discussed. Generally, further increase of excitation power from the onset power for EEA causes photoinduced blinking, and the increase of excitation power finally results in photoinduced bleaching. In this thesis, SWCNTs were exposed to high atmospheric ion flux generated by corona discharge in order to verify the effect of atmospheric ions to photoinduced degradation. As a result, photoinduced bleaching of PL was observed at the excitation power much lower than the onset of photoinduced bleaching in natural environment. Atmospheric ions exist, though sparse, all the time in air. Therefore, atmospheric ions is the candidate for the origin of photoinduced degradation in air. Hydronium ion was attributed to the major chemical species causing the degradation by atmospheric ions because of the stability of hydronium ion in air and more preferential reaction of pi-electron network and cation than anion. The role of oxygen to the mechanisms of the reaction between atmospheric ions and SWCNTs was proposed from the similarity to the bleaching in acidic solution. Förster resonant energy transfer between excitons in SWCNTs and

oxygen was attributed to the reason for photoinduced effect. Although the recovery from degraded PL using annealing in Ar/H<sub>2</sub> atmosphere was examined, full recovery was not achieved at this time. Further study for the recovery is needed in this regard.

This thesis provided mainly three new topics, first observation of well-defined diffusion length, onset power for EEA, and the origin of photoinduced degradation. Those topics were discussed from relating PL experiments results. However, there are still points to check out. For example, although suspended SWCNTs is more intrinsic than surfactant wrapped SWCNTs, there is the concern that SWCNTs in chapter 3 was somewhat affected by atmospheric ions. Along with the establishment of recovery method from degraded SWCNT, intrinsic diffusion length of exciton in SWCNTs should be further examined. If the quench point for excitons were already induced in SWCNTs in chapter 3 and can be removed by annealing as GO reduced, exciton diffusion length will further be extended. It is also unclear that the photoinduced degradation is due to the attachment of hydronium ion. The assignment of the origin for photoinduced degradation is based on many assumption. Clear evidence for the assignment is needed. In addition to the assignment of the origin, precise mechanisms should be established for revealing onset power for photoinduced degradation.

If knowledge for photoinduced degradation progresses, then nano-scale modification of SWCNTs will be available with a combination of photoinduced effect and near-field technique. Those technique will contribute to open up a new scientific field and technology. Intense PL emission from ozonized SWCNTs [1], which is achieved by photoinduced reaction, and observation of photon antibunching in PL from SWCNTs [2] are good examples for the possibility of modified SWCNTs. Those phenomena are both explained by exciton localization due to extrinsic effects.

Mobile information traffic in 2014 was thirty times larger than whole internet traffic in 2000, and mobile information traffic will reach 10 times of that in 2014 for next 5 years [3]. Energy consumption for the network devices will also increase as information traffic does. On the other hand, the size of batteries for mobile network devices will be miniaturized with the development of wearable devices. The technology which will be achieved by the nanotube science satisfies quite a few demands for future mobile network. The present work contributes to the development of such technology.

## Reference

- [1] S. Ghosh, S. M. Bachilo, R. A. Simonette, K. M. Beckingham, and R. B. Weisman, *Science* 330, 1656 (2010).
- [2] W. Walden-Newman, I. Sarpkaya, and S. Strauf, *Nano Lett.* 12, 1934 (2012)
- [3] Cisco Visual Networking Index: Global Mobile Data Traffic Forecast Update 2014–2019 White Paper, Cisco Systems, Inc., United States (2015)

# Acknowledgements

The author wish to thank Prof. Y. Homma for his support starting from 2009 when the author joined his laboratory as a bachelor student. Especially, his attitude toward education in which he does not give up teaching uncomprehending students like the author is worth following. The author now believes the choice that the author starts to research on SWCNTs in his laboratory was better than any others.

The author wish to thank Dr. S. Chiashi for his support during 2009 to 2010 when he had worked in Y. Homma's laboratory as an assistant professor.

The author wish to thank Dr. J. Xie for his support during 2010 to 2012 when he had worked in Y. Homma's laboratory as a postdoctoral researcher.

The author wish to thank Dr. H. Hibino and Dr. H. Omi for their supports while the author had joined Low-Dimensional Nanomaterials Research Group in NTT Basic Research Laboratory from 2010 to 2011.

The author wish to thank Dr. K. Asakawa, Dr. T. Inoshita, Dr. M. Ichida, and Dr. M. Yokokawa for their supports while the author had joined Tsukuba Nanotechnology Human Resource Development Program from 2012 to 2014.

The author wish to thank stimulating discussions with Dr. M. Takayama, Dr. M. Banno, Dr. S. Konabe, and Dr. S. Chiashi for chapter 4 in this thesis. In addition, the work shown in chapter 4 was partially supported by a Grant-in-Aid for Scientific Research on Priority Area (No. 19054015) from the Ministry of Education, Culture, Sports, Science and Technology (MEXT) of Japan.

# Appendix

## Full Python Script for Monte Carlo Simulation

```
#-----
# -*- coding: UTF-8 -*-
# Name:      EEA_007
# Purpose:   Random Walk Simulation of Exciton-Exciton Annihilation
# Author:    Takumi
#
# Created:   011/06/2015
# Copyright: (c) Takumi 2015
# Licence:   <your licence>
#-----

import time
import math
import random
from multiprocessing import Process, Queue
from Scripts.Completed.PrivateModule import OverWrite
from Scripts.Completed.PrivateMathModule import Transpose
import matplotlib.pyplot as plt

def main():
    For7Threading()

def For7Threading():
    #Function processing queue for multithreading technique.

    #Maximum laser power ( $\mu$ W)
    MLP = 100

    result = []

    for i in range(MLP/70):

        print i*7+10, "to", i*7 + 70

        q = Queue()

        thread_00 = Process(target=LaserPowerDependence, args=(q, i*35+10,))
        thread_01 = Process(target=LaserPowerDependence, args=(q, i*35+20,))
        thread_02 = Process(target=LaserPowerDependence, args=(q, i*35+30,))
        thread_03 = Process(target=LaserPowerDependence, args=(q, i*35+40,))
        thread_04 = Process(target=LaserPowerDependence, args=(q, i*35+50,))
        thread_05 = Process(target=LaserPowerDependence, args=(q, i*35+60,))
        thread_06 = Process(target=LaserPowerDependence, args=(q, i*35+70,))

        thread_00.start()
        thread_01.start()
        thread_02.start()
        thread_03.start()
        thread_04.start()
        thread_05.start()
        thread_06.start()
```

```
q.get()
q.get()
q.get()
q.get()
q.get()
q.get()
q.get()
q.get()
```

```
time.sleep(3600 * 24)
```

```
def LaserPowerDependence(Queue, power):
```

```
    time_start = time.time()
```

```
    #Call physical parameter class
    C = Const()
```

```
    #Total simulation time (count down)
    time_tot = C.time_tot
```

```
    #The variable "time_gen" is the time duration for exciton generation
    #The variable "time_gen" is tuned referring the variable "power" based on the typical exciton generation time of 59 ps at 100 μW.
    time_gen = (C.time_gen * (100.0/power))
```

```
    #Number of excitons generated during simulation.
    N = int((C.time_tot/C.time_gen) * (power / 100.0))
```

```
    #Definition of quench point
    #The first quench point is automatically set at an edge of SWCNT.
    N_Defect = int(C.len_tot/C.len_diffect)
    QP = [int(i * C.len_diffect/C.len_div) for i in range(N_Defect)]
```

```
    #List for exciton instances
    exc = []
```

```
    #List for decay paths of each exciton instances
    result = []
```

```
    #Definition of each exciton instances.
    for x in range(N):
        #Labeling exciton instances
        exc.append("exc_"+str(x))
        #Definition of exciton instances
        #(Speed, Radiative decay time, Rethermalization time, Nanotube length, Cell length, 1σ of excitation laser)
        exc[x] = Exciton(C.v, C.time_radiative, C.time_rethermal, C.len_tot,C.len_div, C.len_laser)
        #Temporal results for all excitons are set to "R" meaning radiative decay.
        #Other results will be overwrote later.
        result.append("R")
```

```
    #Generation of first exciton.
    exc[N-1].Generation()
    N = N - 1
```

```
    #Trigger the simulation
    while time_tot > 0:
        time_tot = time_tot - C.time_div
```

```

#Management of exciton generation
if time_gen <= 0 and N >= 1:
    #Generation of new exciton instance
    exc[N - 1].Generation()
    N = N - 1
    #Reset the variable "time_gen"
    time_gen = (C.time_gen * (100.0/power))
else:
    #If not, continue the countdown of the variable "time_gen"
    time_gen = time_gen - C.time_div

#For all exciton instances defined,
for x in range(len(exc)):
    #Call aging method if positive radiative decay time.
    if exc[x].proxy_t_r > 0:
        exc[x].Aging(C.time_div)

    #If the position of an exciton instance is out of area, call relaxation method.
    if not(0 <= exc[x].pos/C.len_div <= C.len_frame):
        exc[x].Relaxation()
        result[x] = "END"
        break

    #Decision of EEA
    for i in exc:
        if not(exc[x] == i) :
            if i.proxy_t_r > 0:
                if int(exc[x].pos/C.len_div) == int(i.pos/C.len_div):
                    exc[x].Relaxation()
                    result[x] = "EEA"

    #Decision of nonradiative decay at quench points
    for i in QP:
        if int(exc[x].pos/C.len_div) == i:
            exc[x].Relaxation()
            result[x] = "QP"
            break

#Followings are data processing
OutPut = [[str(power), str(result.count("R")), str(result.count("QP")), str(result.count("END")), str(result.count("EEA"))]]
OverWrite("C://Users/T.Inaba/Desktop/EEA_4Thesis002.asc", OutPut)

print power, "end"
time_end = time.time()
time_tot = time_end - time_start
print "Simulation time (s): " + str(time_tot)

#For multithreading technique
Queue.put(power)

def VisualExciton():

    time_start = time.time()

    C = Const()

    time_tot = C.time_tot

```

```

time_gen = C.time_gen

N = int(C.N_tot)

N_Defect = int(C.len_tot/C.len_diffect)
QP = [int(i * C.len_diffect/C.len_div) for i in range(N_Defect)]

exc = []
result = []
for x in range(N):

    exc.append("exc_"+str(x))
    exc[x] = Exciton(C.v, C.time_radiative, C.time_rethermal, C.len_tot, C.len_div, C.len_laser)
    result.append([])

exc[N - 1].Generation()
N = N - 1

while time_tot > 0:
    time_tot = time_tot - C.time_div

    if time_gen <= 0 and N >= 1:
        exc[N - 1].Generation()
        N = N - 1
        time_gen = C.time_gen
    else:
        time_gen = time_gen - C.time_div

    for x in range(len(exc)):
        if exc[x].proxy_t_r > 0:

            exc[x].Aging(C.time_div)
            result[x].append([time_tot * C.time_unit * (10 ** 9), exc[x].pos * C.a0 * (10 ** 9)])

            if not(0 <= exc[x].pos/C.len_div <= C.len_frame):
                exc[x].Relaxation()
                result[x].append([time_tot * C.time_unit * (10 ** 9), exc[x].pos * C.a0 * (10 ** 9)])
                break

            for i in exc:
                if not(exc[x] == i) :
                    if i.proxy_t_r > 0:
                        if int(exc[x].pos/C.len_div) == int(i.pos/C.len_div):
                            i.Relaxation()

            for i in QP:
                if int(exc[x].pos/C.len_div) == i:
                    exc[x].Relaxation()
                    result[x].append([time_tot * C.time_unit * (10 ** 9), exc[x].pos * C.a0 * (10 ** 9)])
                    break

time_end = time.time()
time_tot = time_end - time_start
print "Simulation time (s): " + str(time_tot)

for element in result:
    x = Transpose(element)[0]

```

```

y = Transpose(element)[1]
plt.plot(x,y)

```

```

#For the line plot of quench point

```

```

QP_x = [0, C.time_tot * C.time_unit * (10 ** 9)]
QP_y = [[i*C.len_div * C.a0 * (10 ** 9),i*C.len_div * C.a0 * (10 ** 9)] for i in QP]
for i in QP_y:
    plt.plot(QP_x, i, color = "black", linestyle = "--")

plt.ylim(0, C.len_frame * C.len_div * C.a0 * (10 ** 9))
plt.xlim(0, C.time_tot * C.time_unit * (10 ** 9))
plt.show()

```

```

def TestDiffusionLength():

```

```

    time_start = time.time()

```

```

    C = Const()

```

```

    result = []

```

```

    n = 1000

```

```

    for x in range(n):

```

```

        exc = Exciton(C.v, C.time_radiative, C.time_rethermal, C.len_tot,C.len_div)
        # Generation_Zero() method generates exciton instances at the center of the nanotube.
        exc.Generation_Zero()
        #Continue calling aging method till radiative decay.
        while exc.proxy_t_r > 0:
            exc.Aging(C.time_div)
        #Convert the step of position into the unit of nm.
        pos = int(exc.pos*C.a0*(10**9))
        result.append([pos])
        print n - x

```

```

    #output the result

```

```

    Export("C://Users/Takumi/Desktop/160319DoctorThesis/Data/Chap.4/150602EEASim/data/EEA_017.csv", result)

```

```

    time_end = time.time()

```

```

    time_total = time_end - time_start

```

```

    print time_total

```

```

class Const:

```

```

    #All parameters are defined here.

```

```

    def __init__(self):

```

```

        self.a0 = 5.292 * (10 ** -11.0) #Unit length in meter
        self.me = 9.109 * (10 ** -31.0) #Unit weight in kilo gram.
        self.hbar = 1.055 * (10 ** -34.0) #Dirac constant in the unit of J·s.
        self.Eh = 4.360 * (10.0 ** -18.0) #Unit energy in Joule
        #Followings are derived unit
        self.time_unit = self.hbar/self.Eh #Unit time in seconds
        self.absT = 1.0 #Unit of temperature in K.

```

```

    #Followings are parameters for the definition of exciton speed.

```

```

    self.m = 0.17 #The effective mass of an exciton. Ref. D. M. Harrah

```

```

self.kb = 1.380 * (10.0 ** -23.0) * ((1.0/self.Eh)/(1.0/self.absT)) #Boltzmann constant
self.T = 300 * (1/self.absT) #Temperature
self.v = 0.15 * math.sqrt(self.kb*self.T/self.m) #Speed of an exciton (1σ of Gaussian distribution)
#The relation between rate constant and diffusion length
#1: 1311 nm
#0.1: 127 nm

#Followings are time relating parameters
self.time_radiative = 1 * (10 ** -9.0) * (1/self.time_unit) #Radiative decay time
self.time_rethermal = 40 * (10 ** -15.0) * (1/self.time_unit) #ReThermalization time
self.time_gen = 0.059 * (10 ** -9.0) * (1/self.time_unit) #Duration time for the generation of a new exciton instance
#59ps at 100 μW
self.time_tot = 500 * (10 ** -9.0) * (1/self.time_unit) #Total simulation time

self.time_div = 20 * (10 ** -15) * (1/self.time_unit) #Redefine the unit time because atomic unit is needlessly precise.
self.time_frame = self.time_tot/self.time_div #Representation of total simulation time in frame.

self.N_tot = self.time_tot/self.time_gen #Number of total exciton instances

#Followings are length relating parameters
self.len_tot = 0.8 * (10 ** -6.0) * (1/self.a0) #Nanotube length
self.len_div = 2.0 * (10 ** -9.0) * (1/self.a0) #Coherent length of exciton instances
self.len_frame = self.len_tot/self.len_div
self.len_diffect = 0.8 * (10 ** -6.0) * (1/self.a0)
#The generation point of exciton instances are determined by Gaussian distribution.
self.len_laser = 0.8 * (10 ** -6.0) * (1/self.a0)

```

class Exciton:

"""

This class generate exciton instances.

The physics of exciton diffusion is treated in this class.

This class treat the generation, diffusion, and annihilation of exciton instances.

The position of exciton instances are returned when each one of methods are called.

Basically, time and position are treated as float number in exciton instances.

Time or position are converted an integer number when the value is returned.

Arguments: (Spee, Radiative time, Rethermalization time, Nanotube length, Unit length of the nanotube)

"""

def \_\_init\_\_(self, v, time\_radiative, time\_rethermal, len\_tot, len\_div, len\_laser):

self.v = v

self.time\_radiative = time\_radiative

self.time\_rethermal = time\_rethermal

self.len\_tot = len\_tot

self.len\_div = len\_div

self.len\_laser = len\_laser

#Radiative time is set to zero till the call of generation method.

self.proxy\_t\_r = 0

#Method treating the generation of exciton instances

def Generation(self):

#The generation position of exciton instances is based on Gaussian distribution.

self.pos = random.gauss(self.len\_tot/2.0, self.len\_laser)

#Radiative decay time

self.proxy\_t\_r = self.time\_radiative

```

#Initial rethermalization time
self.SetProxy_ret()
#Initial speed
self.SetProxy_v()

return int(self.pos/self.len_div)

# Method treating the generation of exciton instances at the center of axis.
def Generation_Zero(self):
    #Generation position of exciton instances
    self.pos = 0
    self.proxy_t_r = self.time_radiative
    self.SetProxy_ret()
    self.SetProxy_v()

    return int(self.pos/self.len_div)

#Method treating random walk motion of exciton instances
def Aging(self, time_div):
    #Radiative decay time decreases when Aging method is called.
    self.proxy_t_r = self.proxy_t_r - time_div

    #Followings are scripts relating to rethermalization of exciton instances.
    if self.proxy_ret <= 0:
        #Test for the rethermalization time remaining
        self.SetProxy_v()
        #New speed is got as rethermalization.
        self.SetProxy_ret()
        #New rethermalization time is got as rethermalization
    else:
        self.proxy_ret = self.proxy_ret - time_div
        #If not, rethermalization time decrease.

    self.pos = self.pos + self.proxy_v * time_div
    #Move to new position as the call of Aging method
    return int(self.pos/self.len_div)

def SetProxy_ret(self):
    self.proxy_ret = random.gauss(self.time_rethermal, self.time_rethermal*0.1)

def SetProxy_v(self):
    #If radiative time is zero (decay), set the speed of the exciton instance to zero.
    if self.proxy_t_r == 0:
        self.proxy_v = 0
    #Gaussian distribution of the speed of exciton instances.
    else:
        self.proxy_v = random.gauss(0, self.v)

#If Relaxation method is called, set radiative decay time to zero.
def Relaxation(self):
    self.proxy_t_r = 0

    return int(self.pos/self.len_div)

if __name__ == '__main__':
    main()

```

### Detail of Monte Carlo Simulation in Chapter 3

The script was operated on Python 2.7. Python Scriptor 2.6.0.0 was employed for integrated development environment (IDE). The script was composed of mainly 7 sections.

#### i. Main Function

The function to be execute was set here. For example, For7Threading which executes LaserPowerDependence function with multithreading technique function was selected above.

#### ii. For7Threading Function

This function was bundled with LaserPowerDependence function. The execution of LaserPowerDependence function for Fig. 3.9 takes huge time. Therefore, the use of multithreading technique is necessary for cutting down execute time. The central processing unit (CPU) employed for executing the script could handle 8 thread simultaneously. However, only 7 of those was used here for stable operation. Each one of threads got a laser power from 1-100  $\mu\text{W}$  corresponding to plot points in Fig. 3.9, run LaserPowerDependence function, and generated results for each laser power. Although multithreading technique was employed here, it took two weeks to get whole results in Fig. 3.9. Long execute time may be because Python is the script language. Especially, it is known that the use of for loop in the Python scripts significantly elongate the execute time. Actually, programing language is more favorable for cutting down execute time.

#### iii. LaserPowerDependence Function

LaserPowerDependence function got excitation power from For7Threading function, and generated each plot point in Fig. 3.9. In the function, several number of exciton instances were generated with 1D degree of freedom for their movements. The generation of every single exciton instances had the time interval. The generation rate “time\_gen” was determined from the excitation power. After the first generated exciton instance started to diffuse, the countdown for generating the second one also started. Then, the second exciton started to diffuse when the countdown finished, thus time\_gen = 0.

The valuable time\_gen was corresponding to the excitation intensity of a SWCNT. Considering that the SWCNT is excited by laser light with the wavelength of 785 nm and the laser intensity of 100  $\mu\text{W}$ , integrated photon flux of the laser light is  $I = 3.95 \times 10^{14}$  photons/s. If spot shape of the laser light is 2D Gaussian with  $\sigma = 0.8 \mu\text{m}$  for each directions, photon flux along the nanotube axis is;

$$F(x) = I \frac{1}{\sqrt{2\pi\sigma^2}} f(x) \quad (\text{A.1})$$

where  $f(x)$  is 1D normal distribution function. Here,  $y$  dependence of photon flux is vanished due to the substitution of  $y = 0$  into 2D Gaussian function. Considering absorption cross section per unit length  $\sigma_{22} = 85 \text{ nm}^2/\mu\text{m}$  [1][2], the number of photons absorbed by a segment  $dx$  per unit time can

be written as;

$$dN_{abs} = \sigma_{22}F(x)dx \quad (A.2)$$

Integration of Eq. A.2 for infinity length gives the number of photons absorbed per unit time  $N_{abs}$ .

$$N_{abs} = \frac{I\sigma_{22}}{\sqrt{2\pi}\sigma^2} \quad (A.3)$$

The value of  $N_{abs}$  is  $1.67 \times 10^{10}$  photons/s. Therefore, when the SWCNT is excited by laser light having the wavelength of 785 nm and the laser intensity of 100  $\mu$ W, the valuable “time\_gen” is equal to 59 ps. The initial position of excitons are determined following Gaussian probability dispersion function with  $\sigma = 0.8 \mu\text{m}$ .

Four decay path ways were assumed for exciton instances in the script. First one was radiative decay which was got when the exciton instances survives for radiative decay time of 1 ns. Others were all non-radiative decay due to end quenching at the edge of the SWCNT, quenching points which could be set in the SWCNT, and EEA process. Although quench points was assumed in the scripts, that decay was not employed for Fig. 3.9.

#### iv. VisualExciton Function

VisualExciton function generated Fig. 3.8 for verifying the successful diffusion of exciton instances. Major process for generating the result was similar to LaserPowerDependence function, but the results were more visualized.

#### v. TestDiffusionLength Function

TestDiffusionLength function generated Fig. 3.8 in order to set the speed of exciton instances for every steps. The speed of exciton was adjusted so that diffusion length equal to intrinsic diffusion length. Major process for generating the result was similar to LaserPowerDependence function, but the initial position of exciton instances were fixed at the center of the axis.

#### vi. Const Class

Const class handle physical constant and parameter for the simulation.

#### vii. Exciton Class

Exciton class handle the dynamics of exciton instance.

### Reference

- [1] M. F. Islam, D. E. Milkie, C. L. Kane, A. G. Yodh, and J. M. Kikkawa, Phys. Rev. Lett. 93, 037404 (2004)
- [2] S. Berciaud, L. Cognet, and B. Lounis, Phys. Rev. Lett. 101, 077402 (2008)